Journal of
Instrumentation

PAPER • OPEN ACCESS

Study on discharge and short circuit generation in CMS GE1/1 triple-GEM detectors during Run 3

To cite this article: M. Abbas *et al* 2025 *JINST* **20** P05035

Published by IOP Publishing for Sissa Medialab

Received: *October 31, 2024*
Revised: *February 8, 2025*
Accepted: *April 21, 2025*
Published: *May 27, 2025*

Study on discharge and short circuit generation in CMS GE1/1 triple-GEM detectors during Run 3

The GEM group of the CMS collaboration

E-mail: antimo.cagnotta@cern.ch, simone.calzaferri@cern.ch

Abstract: The installation of the new GE1/1 station of Gas Electron Multiplier (GEM) detectors in the Compact Muon Solenoid (CMS) experiment was completed during the Long Shutdown 2 (LS2) phase of the Large Hadron Collider (LHC). The GE1/1 station has been operational in the CMS detector since the beginning of the Run-3 data-taking phase, and for the first time the GEM technology was deployed on a large scale, comprised of 144 chambers and tested in running conditions as integral part of the CMS data acquisition, reconstruction, and analysis chain. The deployment of the GEM detector required careful planning throughout the years, posing several challenges of practical and conceptual nature in integrating an entirely new subsystem in the existing CMS frame. Operations on the other hand provided a unique opportunity to test the GEM technology in never-before seen conditions, and an occasion to study their behavior during data taking.

In describing some of the solutions to the posed challenges and the findings during the data-taking, the article will focus on the aspects related to power system management, including high-voltage and current monitoring, which is intrinsically related to the response of the chamber due to the workings of the GEM foil charge flow. To this end, this article will illustrate the operations of GE1/1 detectors in the first two years of Run-3, with a particular focus on the analysis of discharge occurrences, on the generation of short circuits in GE1/1 GEM foils and on the adopted mitigation strategies. The applied layout of the GEM detectors is thoroughly described, and detailed operating conditions of the detectors are discussed, along with the actions taken to mitigate these events.

Keywords: Electron multipliers (gas); Gaseous detectors; Micropattern gaseous detectors (MSGC, GEM, THGEM, RETHGEM, MHSP, MICROPIC, MICROMEGAS, InGrid, etc)

https://doi.org/10.1088/1748-0221/20/05/P05035

2025 JINST 20 P05035

Contents

2025 JINST 20 P05035

1 Introduction

The muon system of the Compact Muon Solenoid (CMS) experiment [1] was upgraded during the Long Shutdown 2 (LS2) phase of the Large Hadron Collider (LHC) program [2]. The upgrade included the installation of a new station in the muon spectrometer based on the Gas Electron Multiplier (GEM) [3] technology, and in specific triple-GEM foil detectors. The station is called GE1/1, and it consists of two wheels of chambers in both the endcaps of CMS. This station is shown in figure 1, portraying a quadrant of the muon spectrometer. In the same figure, the other detector stations of the muon system are shown, which include detectors using Drift Tubes (DT), Resistive Plate Chambers (RPC), and Cathode Strip Chambers (CSC) technologies [1].

GEM detectors belong to the category of Micro Pattern Gas Detectors (MPGDs) [4]. Their installation in CMS is intended to enhance the capability of the CMS detector to trigger upon and reconstruct high-η muons, extending its overall physics reach and improving the selection efficiency of ongoing physics searches. In figure 1.2 in [5], the single muon trigger rate curves before and after the GE1/1 upgrade for the region $1.6 < |\eta| < 2.2$ are shown. With the upgrade, the L1 muon trigger thresholds can be maintained at low p_T values, keeping high the efficiency for capturing interesting physics processes featuring soft leptons.

A key benefit of upgrading CMS with the installation of GEM detectors is their ability to enhance muon detection and triggering efficiency in the high pileup scenario foreseen for the High Luminosity phase of the LHC [6]. The pileup increase implies indeed a greater complexity of reconstruction of proton-proton collision events, potentially degrading the performances. The complete GEM project consists of installing three GEM stations (GE1/1, GE2/1, and ME0) in the forward region of CMS. This also increases the redundancy of the muon system and extends its acceptance up to $|\eta| = 2.8$, as illustrated in [7]. The choice of GEM technology was driven by its robustness against radiation and its precision in both temporal and spatial resolution. This also dictated the layout and position in CMS of GEM chambers, and of the services necessary for its regular operation. Details on the GE1/1 layout, operational principles, and the power distribution system are described in the sections 1.1, 1.2, 2 respectively. One description in detail of the manufacturing process and quality control can be found in [8–10].

The new station is composed of 144 modules, or chambers, which are paired in 72 super-chambers. Each super-chamber is composed of two modules and divided into 36 super-chambers at each endcap. The GE1/1 station provides two position measurements by pairing two individual modules into a super-chamber as described in [5], and therefore each endcap comprises 36 super-chambers. The two modules of each super-chamber are referred to as Layer 1, installed closer to the interaction point, and Layer 2. Due to mechanical constraints of the CMS detector, trying to maximize the detector area and ensuring the space needed to fit the services for the detectors' functioning, two slightly different length models of GE1/1 super-chambers have been produced: long (GE1/1-L) and short (GE1/1-S). Once installed, they alternate in the azimuthal plane as shown in figure 2 with the mechanical structure that limits the detector dimensions. The chambers have a trapezoidal shape and each of the 36 super-chambers per endcap subtend an angle of 10.15° giving full azimuthal coverage in a staggered pattern that includes an overlap of 2.6 mrad. The specifications for the geometrical parameters of the chambers are listed in table 1.

Table 1. Geometrical parameters of the two version of GE1/1 chambers: short (GE1/1-S) and long (GE1/1-L). Reproduced from [5]. CC BY 4.0.

Trapezoid parameter (active volume)	GE1/1-S	GE1/1-L
Longitudinal length (cm)	106.1	120.9
Short basis (cm)	23.1	23.1
Long basis (cm)	42.0	44.6
Thickness (cm)	0.7	0.7

2025 JINST 20 P05035

1.1 Scope of GE1/1 and functioning of GEM technology

The GE1/1 detector helps to track, identify, and measure the muon bending angle with respect to the adjacent Cathode Strip Chamber (CSC). By integrating the measurement of the bending angle into the first trigger level (L1) system [11] the efficiency to select muons can be kept high while keeping the L1 rate constant. The momentum resolution is increased by the more precise measurement of the muon bending angle thanks to the angular resolution of 300 µrad [5] of the GE1/1 detectors. The GEM station will play an important role in the High Luminosity phase of the LHC [6], where these unique characteristics will be crucial for the performance of the L1 trigger. The GEM detector sandwiches three GEM foils between a cathode (or Drift) plane and an anode readout plane, numbered in order as GEM1, GEM2, and GEM3. The planes are separated by thin gas gaps, referred as Drift for the gap between cathode and GEM1, Transfer 1 between GEM1 and GEM2, Transfer 2 between GEM2 and GEM3, and Induction gap between GEM3 and the anode readout plane. The schematics showing the structure of the electrodes stack in triple-GEM detectors is displayed in figure 3, while the thicknesses of the four gas gaps are listed in table 2.

A GE1/1 GEM foil is a 50 µm thin polyimide foil with 5 µm copper-coated faces. During the manufacturing, the foil gets perforated with microscopic holes by chemical etching. The holes have a truncated double cone shape, with an outer and inner diameter of 70 µm and 50 µm respectively. In addition, the holes are arranged in an hexagonal pattern and they are spaced with a pitch of 140 µm.

When an ionizing particle enters the gas medium, it ionizes atoms in the gas and generates primary ionization electrons. These are then accelerated by the intense electric field present inside the GEM holes, thus creating secondary ionization electrons, producing an avalanche multiplication of the primary ionization signal, which grows while crossing the GEM foils and being transported across the gas gaps [3].

The avalanche multiplication of the primary ionization electrons can achieve a high amplification gain of up to 10^5 by applying a modest voltage ($\sim$ 400 V) between the two faces of each GEM foil in the stack. The multiplied charge is collected by 3072 readout copper strips, clustered in groups of 128 channels. In particular, we have three groups along the ϕ-coordinate and eight along the η-coordinate. Each of the 24 readout groups is read by one VFAT3 front-end chip, a trigger and tracking ASIC that is specially designed to read out the signal from groups of 128 strips in the GEM detectors in the CMS, including the condition they will have to endure during the High Luminosity LHC phase. A detailed description of the VFAT3 chip can be found in [12]. The services required to operate a GE1/1 detector properly include:

- gas mixture Ar/CO_2 (70/30), with a renewal rate of 0.5 detector volumes per hour in an open loop. The gas exiting from the detector is not recirculated;

- High Voltage (HV), needed to multiply and transport the electrons produced during the primary ionization by a particle traversing the gas medium. This is provided by multichannel power supply boards (CAEN A1515BTG [13]): their main characteristic is that they have 14 independent channels. To power a single module, seven of them are needed. This feature offers flexibility for the setting of the potential difference between each plane of the stack of a triple-GEM detector. The board ensures a current resolution of 100 pA when the delivered current is below 100 µA. Otherwise, the resolution is 1 nA.

2025 JINST 20 P05035

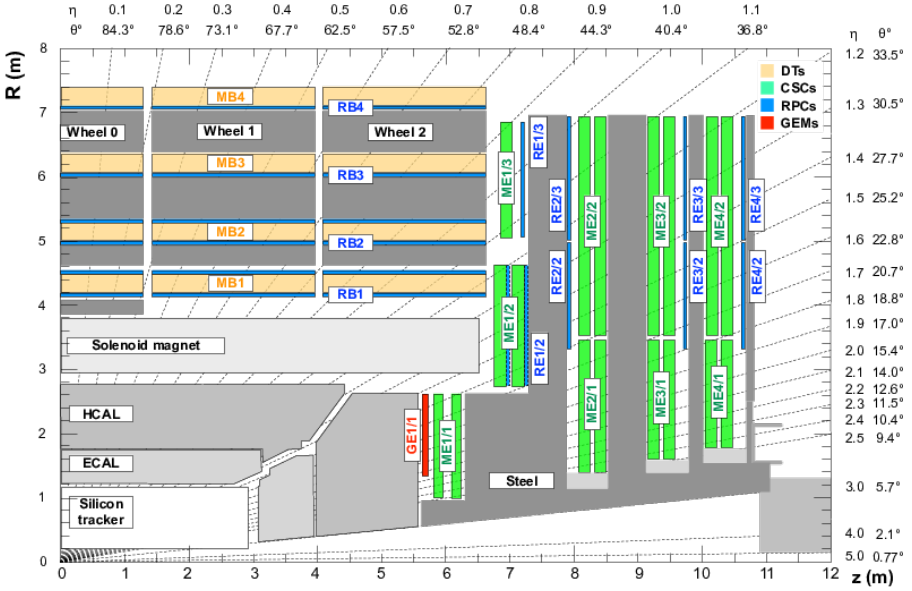

Figure 1. A quadrant of the CMS detector, showing the different types of chambers used in the muon system [1]. The original system consisted of the DT chambers (yellow) in the barrel region, together with the RPCs (light blue) and CSCs (green) in the endcap regions. The new GEM detector station GE1/1 is indicated in red. Reproduced from [5]. CC BY 4.0.

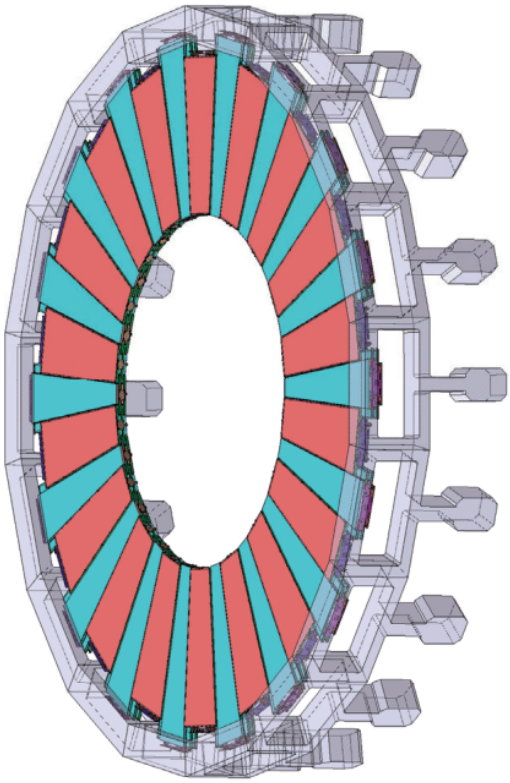

Figure 2. Schematic view of the GE1/1 super-chambers once installed in CMS, characterised by a staggered arrangement. Detectors in red (dark in monochrome print) identify the short detector module, while those in blue (light in monochrome print) identify the long ones. Reproduced from [5]. CC BY 4.0.

2025 JINST 20 P05035

- Low Voltage (LV), to power the readout electronics. This is provided by CAEN A3016-HP boards [14];
- Cooling water, with a temperature of 16 °C and a pressure of 9 bar, needed for the refrigeration of the front-end detector electronics.

Table 2. Thickness of the gas gaps used for triple-GEM detectors in the GE1/1 station.

Gap	Thickness [mm]
Drift	3
Transfer 1	1
Transfer 2	2
Induction	1

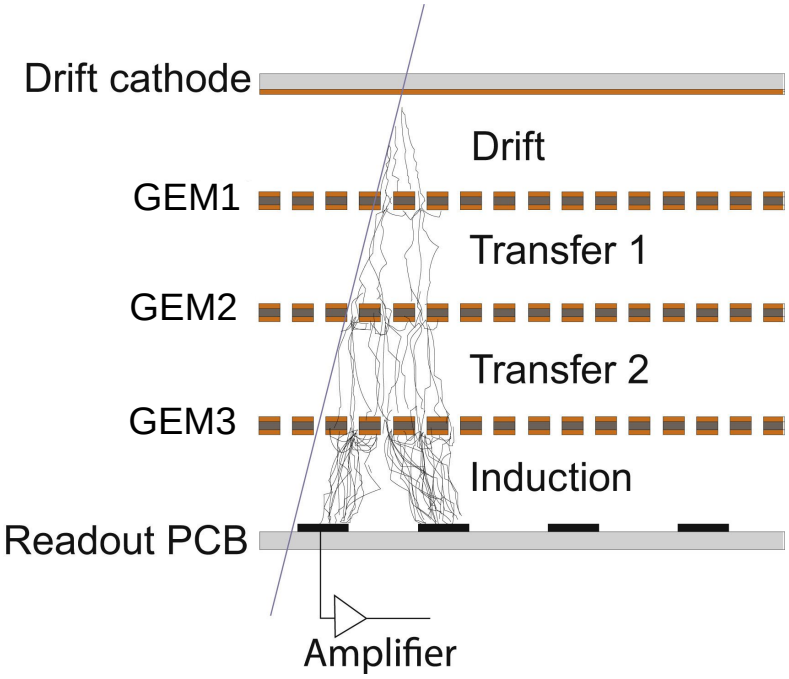

Figure 3. Diagram showing the functioning principle of a triple-GEM detector: an avalanche induced by an ionizing particle crossing the detector develops from the drift gas gap, across the three foils, and generates the signal on the readout copper strips. Reproduced from [7]. CC BY 4.0.

1.2 GEM foils HV distribution in GE1/1

In GE1/1, all the GEM foils have the same trapezoidal design. For each GEM foil, we distinguish between a top face (the side oriented towards the cathode) and a bottom face (oriented towards the readout plane). The top one is segmented in 40 (47) HV sectors of the same area for the GE1/1-S (GE1/1-L) detectors: each segment consists of a copper strip parallel to the narrow side of the trapezoid (a transverse segmentation, with respect to the LHC beampipe). The bottom one is instead a single continuous conductor. In figure 4 the scheme adopted to apply the HV to the foil sectors and the

2025 JINST 20 P05035

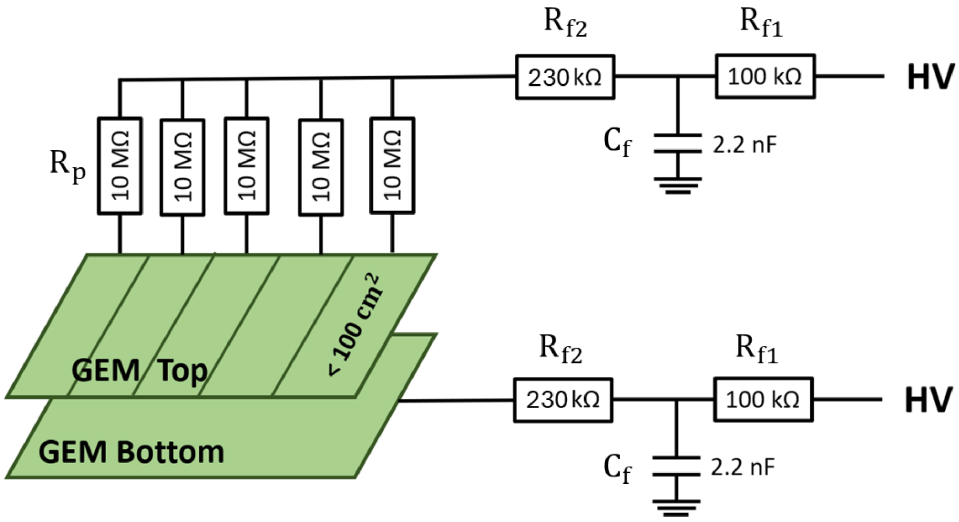

Figure 4. HV distribution schematics from the power supply to a GE1/1 GEM foil. The schema shows the 10 MΩ resistors connected to each HV sector on the top face of the foil (called protection resistors R_p), and the 0.33 MΩ HV filter resistors, R_{f1} and R_{f2}, installed between the power supply and each side of the GEM foil. In the HV filter is present also a 2.2 nF capacitor, C_f. Reproduced from [23]. The Author(s). CC BY 4.0.

segmentation is represented. The distribution schema shows the presence of several components between the power supply and the GEM foil: protection resistors (R_p), connected to each HV sector on the top face of the GEM foil, and filter resistors (R_{f1} and R_{f2}), connected on the two faces of the GEM foil, together with a capacitor (C_f), needed to remove the noise given by the power supply.

The size of each HV sector has been designed to have equal area for all of them, going from the narrower to the wider side of the chamber, $\sim 100\,\mathrm{cm}^2$. This design choice is intended to limit the charge that can be drained by the occurrence of a discharge, also limiting its total energy. The distribution schema shows that in the event of a discharge in one sector, the damage would be confined to that sector, thereby protecting the remaining parts of the detector.

1.3 Voltage configuration in terms of equivalent divider current I_{eq}

Henceforth, the HV working point will be indicated with an equivalent divider current I_{eq} value: this value fixes the voltage of each gap, assuming a voltage divider powering the entire detector as shown in figure 5. This convention to label a voltage configuration in terms of I_{eq} is practical to have a unique number for comparison of detector performances.

Table 3 reports the voltage difference applied between each pair of surfaces of the detector stack, followed by the electric field values in the center of each gap and the gain multiplication achieved by setting the whole GEM stack at a given I_{eq}. The HV channels used to power the stack are named as follows:

- Drift, identifies the voltage difference between the cathode plane and the top face of foil GEM1;
- G1Top, the voltage difference between the top and bottom face of foil GEM1;
- G1Bot, the voltage difference between the bottom face of GEM1 and top face of GEM2, generating an electric field in the Transfer 1 gas gap;

- G2Top, the voltage difference between the top and bottom face of foil GEM2;
- G2Bot, the voltage difference between the bottom face of GEM2 and top face of GEM3, generating an electric field in the Transfer 2 gas gap;
- G3Top, the voltage difference between the top and bottom face of foil GEM3;
- G3Bot, the voltage difference between the bottom face of GEM3 and the anode readout plane, generating an electric field in the Induction gas gap.

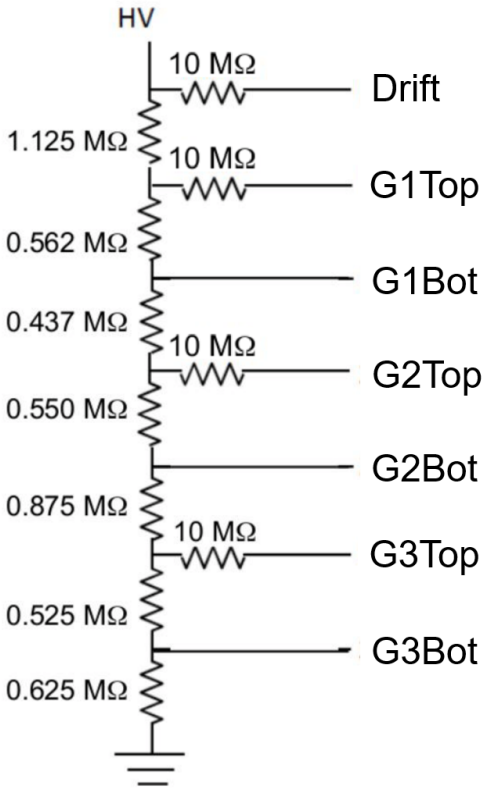

Figure 5. Scheme of the reference resistive divider, which fixes the ratios of voltages applied to the seven HV electrodes. The divider was only used during the quality controls performed during the production of the detector. The voltages proportions have been maintained during the phase of operations in CMS, where the voltage configuration is identified with I_{eq}, the current flowing in this reference resistive divider. On the CMS detector the voltage is provided by multichannel power supply boards CAEN A1515BTG. Reproduced with permission from [9].

2 The GE1/1 HV system

The section is divided into three parts: the first part describes the original design of the HV system, the second part focuses on the phenomena of discharges and trips, and the third part describes the short circuits in a GE1/1 GEM foil. The phenomena described in these section are not exclusive to the GE1/1 station, or GEM detectors in general, but they are common to all MPGDs and represent one of the most critical aspects of their operation [15–17].

Table 3. The top part of the table outlines the voltage difference applied across the GEM foils and gas gaps for a given equivalent divider current I_{eq}. This is not the absolute voltage applied to the electrode, referred to the ground. After the voltages, the corresponding electric fields present inside the GEM foils and gas gaps for a given equivalent divider current I_{eq} are listed. The last line of the table reports the gain achieved setting a given I_{eq} voltage configuration.

Equivalent divider current I_{eq} [µA]	580	690	700	710
Voltage on drift gap [V]	653	776	788	799
Voltage on GEM1 foil [V]	325	387	392	398
Voltage on transfer 1 gap [V]	254	302	307	311
Voltage on GEM2 foil [V]	319	379	385	391
Voltage on transfer 2 gap [V]	508	604	613	621
Voltage on GEM3 foil [V]	305	362	368	373
Voltage on induction gap [V]	363	431	438	444
Electric field in drift gap [kV/cm]	2.18	2.59	2.63	2.66
Electric field in GEM1 foil [kV/cm]	65.0	77.4	78.4	79.6
Electric field in transfer 1 gap [kV/cm]	2.54	3.02	3.07	3.11
Electric field in GEM2 foil [kV/cm]	63.8	75.8	77.0	78.2
Electric field in transfer 2 gap [kV/cm]	2.54	3.02	3.07	3.11
Electric field in GEM3 foil [kV/cm]	61.0	72.4	73.6	74.6
Electric field in induction gap [kV/cm]	3.63	4.31	4.38	4.44
Total gain	$(3.99 \pm 0.14) \cdot 10^2$	$(1.98 \pm 0.08) \cdot 10^4$	$(2.83 \pm 0.11) \cdot 10^4$	$(4.05 \pm 0.17) \cdot 10^4$

2.1 GE1/1 HV system original design

The HV system designed to operate GE1/1 detectors is based on CAEN mainframes SY4527 hosting CAEN A1515BTG boards.

The system is designed to power GE1/1 detectors in pairs, having each group of seven channels powering two GE1/1 detectors, with each board channel group connected to the electrical outlets of a custom made patch panel with a Y splitting cable, as shown in figure 6. In this design, the first and second layer of each GE1/1 super-chamber were powered by the same group of channels. As a consequence, the same electrode of the two layers of a given super-chamber is powered by the same channel in the power supply board (for example, the channel 0 of the A1515BTG board powers both the G3Bot electrodes of the two connected chambers).

2.2 Discharges and trips

One of the potential issues to be accounted for in MPGDs is the occurrence of discharges between the HV powered surfaces inside the detector. A discharge in GEM detectors happens when the density of electrons, produced by the multiplication in a GEM hole, overcomes the Raether limit [18] ($\sim 10^7$ electron-ion pairs) and therefore the streamer regime is reached [3]. This phenomenon has been observed also in GE1/1 detectors during operation and is still under investigation, as well as possible mitigation strategies.

From the HV monitoring point of view, what we have observed are current spikes that lead to recharging of the GEM foil. An example of discharge is shown in figure 7, which shows a current peak at the instant of occurrence of the discharge, followed by an exponential decrease, due to the power supply action which restores the drained charge on the GEM foil. The number of measurements

2025 JINST 20 P05035

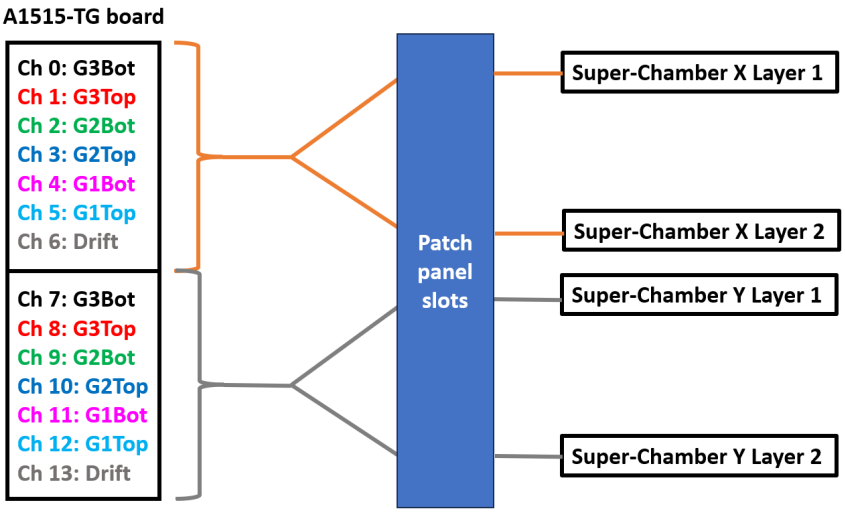

Figure 6. Schematic drawing of the connections from an A1515BTG board to the single detectors. Each board has two groups of seven channels needed to power the seven electrodes of a Triple-GEM detector. In the CMS GE1/1 station, each group of seven channels powers two GE1/1 chambers corresponding to the two layers of a super-chamber.

shown in the plot, and in general in the following study, is limited by the archiving rate performed by the GEM Detector Control System (DCS) [19]. The GEM DCS saves a voltage value every time there is a variation of at least 1 V, while a current value is saved for a variation of at least 0.01 µA.

A protection system is implemented in the A1515BTG board: for each HV channel, a maximum current tolerance I_0 is defined, which can be sustained for a maximum duration, referred to as t_{trip}. If the channel monitored current overcomes I_0 for a time longer than t_{trip}, the HV channel involved gets powered off. This protection power off event is called trip.

The GEM DCS can take up to 3.75 minutes to recover an electrode after a trip. This depends on the voltage to reach (examples are given in table 3) and on the speed of the voltage ramp up (6 V/s for the drift HV channel and 3 V/s for all the others). To obtain the total recovery time, 20 seconds have to be added to the ramp-up time: this offset is the time that the GEM DCS waits after a trip before recovering the channel automatically.

The board trip mechanism is designed to protect the detector from possible damage caused by the energy carried by a discharge, which could involve the front-end electronics or the GEM foils. A discharge can indeed gain energy in case of propagation inside the triple-GEM stack [20].

2.3 Short circuits in a GE1/1 GEM foil

A further potential issue for GEM detectors is the formation of an electrical connection between the upper and lower surfaces of the GEM foil. In the following, this phenomenon is referred to as a "short circuit".

The electrical connection can be generated by the presence of material that gets stuck inside of a GEM foil hole. This can be attributed to a number of factors, including imperfections in the manufacturing process of the foil, the presence of pollutant chemicals within the detector, or the melting of the copper layer, which can occur as a result of elevated levels of discharge activity [15–17].

2025 JINST 20 P05035

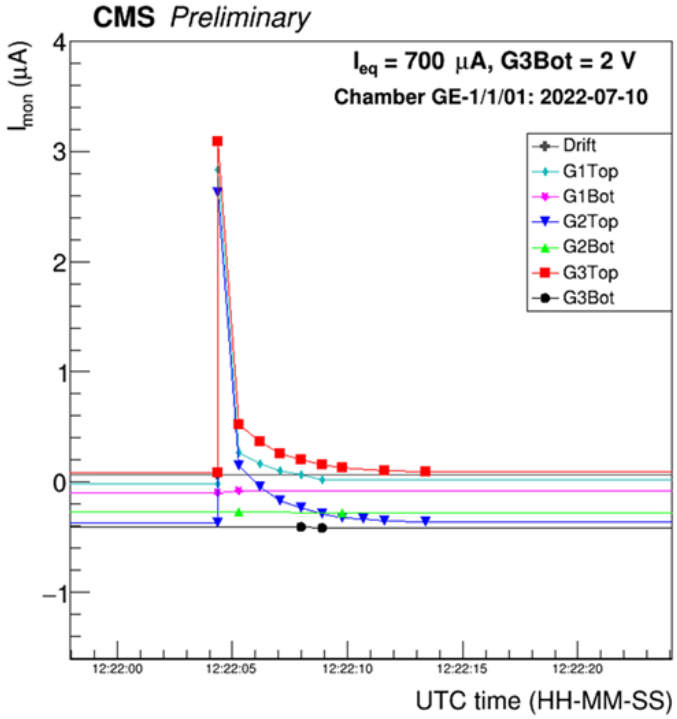

Figure 7. Example of monitored current observed during a discharge event in a GE1/1 detector.

The result of a short circuit is that the two electrodes are at the same potential, which consequently disables the amplification power of the foil. As described in section 1, the top face of the GE1/1 foils is segmented in 40 (47) HV sectors for short (long) chambers. On the contrary, the bottom face of the foil is not segmented. Therefore, the presence of the short circuit connects one top HV sector with the unique copper surface on the bottom side: this design does not imply having a complete deactivation of the amplification on the whole GEM foil but only on the affected HV sector. This de-activated area corresponds to 2.5% (2.1%) of the total surface of a GE1/1-S (GE1/1-L) detector.

Table 4. Summary of electrical components of the HV distribution from the power supply to the GEM foil, depicted in figure 4.

Component	**Value**
Protection resistor (R_p)	10 MΩ
Filter resistor 1 (R_{f1})	100 kΩ
Filter resistor 2 (R_{f2})	230 kΩ
Filter capacitor (C_f)	2.2 nF

During operation, it is crucial to understand the behavior of chambers affected by a short circuit, because a short circuit drains more current than a healthy detector, and the unaffected HV sectors will have a lower voltage than the one set by the power supply. To estimate these voltage values, one can analyze the circuit that powers the entire foil, taking into account the protection resistors R_p and the HV filter resistors R_{f1} and R_{f2}, as shown in figure 4. The values of the resistors are summarized in table 4.

2025 JINST 20 P05035

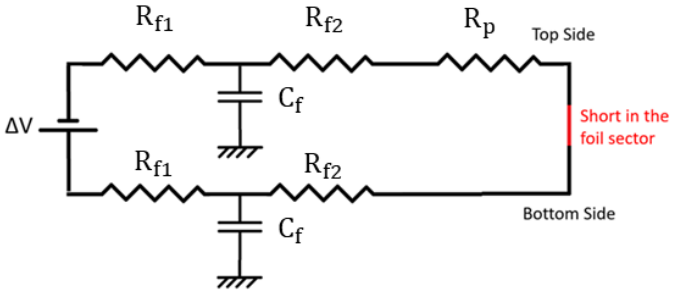

Figure 8. Example of the circuit present between the power supply and the GEM foil in case of a single HV sector affected by a perfectly conductive short circuit. In this case the total resistance present between the power supply and the GEM foil is $R_p + 2(R_{f1} + R_{f2})$, instead of being an open circuit for a GEM foil with no short circuit connection. The values of the components are summarized in table 4. Reproduced with permission from [21].

The circuit formed by the power supply and the GEM foil in presence of a short circuit in a single HV sector is represented schematically in figure 8. The calculation can be done, starting from the non-zero current flowing in the protection resistor of the sector affected by the short circuit. For the remaining protection resistors, only the amplification current flows. This current is approximately 25 times lower than the short circuit current and can be practically zero (few tens of nA) in the absence of background radiation produced by LHC beam collisions. The current seen by the power supply due to the short circuit is the total current flowing in the equivalent circuit. For example, if a single HV sector is affected by a perfectly conductive short circuit and the foil is powered by $\Delta V = 392\,\mathrm{V}$, the current provided by the power supply is $I = \frac{\Delta V}{R_p + 2(R_{f1}+R_{f2})} = 37.0\,\mu\mathrm{A}$. Accordingly, the voltage drop is $\Delta V_{\mathrm{drop}} = 2 \cdot (R_{f1} + R_{f2}) \cdot I = 24.4\,\mathrm{V}$. In conclusion, in this example, the effective voltage applied to the GEM foil is approximately 6 % lower than the voltage provided by the power supply, while the expected current flowing through the HV electrode is around 37 µA.

If the foil has more than one HV sector affected by a short circuit, the total resistance of the circuit generated by the connection is

$$R = 2 \cdot (R_{f1} + R_{f2}) + \frac{R_p}{N_s}, \tag{2.1}$$

where N_s is the number of HV sectors affected by a short circuit. If more than one GEM hole in a given HV sector is affected by a short circuit connection, the current flowing will be the same as in the case of a single hole, if at least one connection is perfectly conductive.

Understanding short circuit dynamics is essential for improving the operational stability of GEM detectors in high-energy physics experiments. The insights gained from this study can inform future design modifications and operational strategies to mitigate short circuit occurrences, enhancing the overall reliability and performance of the detectors.

3 Run-3 operations with beam

This section provides an overview of the main problems encountered during the commissioning of the new GE1/1 station [22, 23], focusing on baseline amplification current during beam collisions and the first two years of operation with the LHC beam.

2025 JINST 20 P05035

3.1 Baseline current in presence of beam

In presence of colliding LHC beams, a non-zero current is observed to flow on each channel of the A1515BTG board due to signal amplification. This effect is particularly noticeable on the G3Top electrode, where the number of incoming avalanche multiplication electrons is much higher than on the other two GEM foils.

A typical representation of the current behavior flowing on the G3Top channel of the A1515BTG board, in the presence of proton-proton (p-p) collisions, is illustrated in figure 9(a). It shows the presence of current spikes, that are a signature of discharges, and a baseline current mirroring the instantaneous luminosity of particle collisions. This can be seen by comparing a zoom of the current plot (figure 9(b)) and the plot showing the instantaneous luminosity of proton-proton (p-p) collisions (figure 9(c)). The amplitude of a discharge is calculated subtracting the baseline current at the corresponding timestamp.

3.2 First year of Run-3 operations with beam

In July 2022, the LHC began producing proton-proton collisions at a center of mass energy $\sqrt{s}$ = 13.6 TeV. At the beginning of 2022 LHC activities, the detectors were operated at the HV working point $I_{\text{eq}} = 700\,\mu\text{A}$.

Since the first LHC fills, as expected for MPGDs [24], the GEM detectors began producing discharges under stable beam operating conditions. On the contrary, the production of discharges decreases after each beam dump, with the chambers basically stopping to produce discharges keeping the HV operating point at the same I_{eq} value used during collisions.

During the first LHC fills, the HV working point I_{eq} was reduced due to frequent discharges and was subsequently adjusted by monitoring the chambers' discharge rate. In addition, G3Bot was deactivated during this phase, to protect the readout electronics and reduce the amount of energy a discharge can gain during a propagation between the planes of the stack.

The behavior of the first part of data-taking of 2022 is summarized by the plots in figure 10 and figure 11.

In the first plot, the average rate of discharges per hour per single chamber is shown. In particular, it is worth noting the evolution of the average from the initial period with an HV working point of $I_{\text{eq}} = 700\,\mu\text{A}$ and a discharge rate of about 18 discharges per hour per single chamber, until the end of August, when the operating point was lowered to 690 µA and the discharge rate decreased by about 94%.

In the second plot, the maximum, minimum, average, and median discharge rate per HV power line — and consequently per pair of chambers — are shown. In the considered period, the discharge rate per HV power line corresponds directly to the discharge rate per super-chamber, as each HV power line supplies one super-chamber. The rate is displayed per pair of chambers because it is not possible to distinguish which module within a pair generated a given discharge, since the pair of chambers is connected to the same HV line, as described in section 2. The data are calculated considering all the HV power lines and thus include 72 values of discharge rate, per each LHC fill analyzed. During this period, one module in a single super-chamber was not connected to the HV. This is the only case where the discharge rate per HV power line is not that of a super-chamber.

In August 2022, the HV working point was set to $I_{\text{eq}} = 690\,\mu\text{A}$, in a first moment with the G3Bot still OFF. After it was observed that the discharge rate was stable, the full stack was powered at $I_{\text{eq}} = 690\,\mu\text{A}$, achieving a discharge rate of around one discharge per single chamber per hour.

2025 JINST 20 P05035

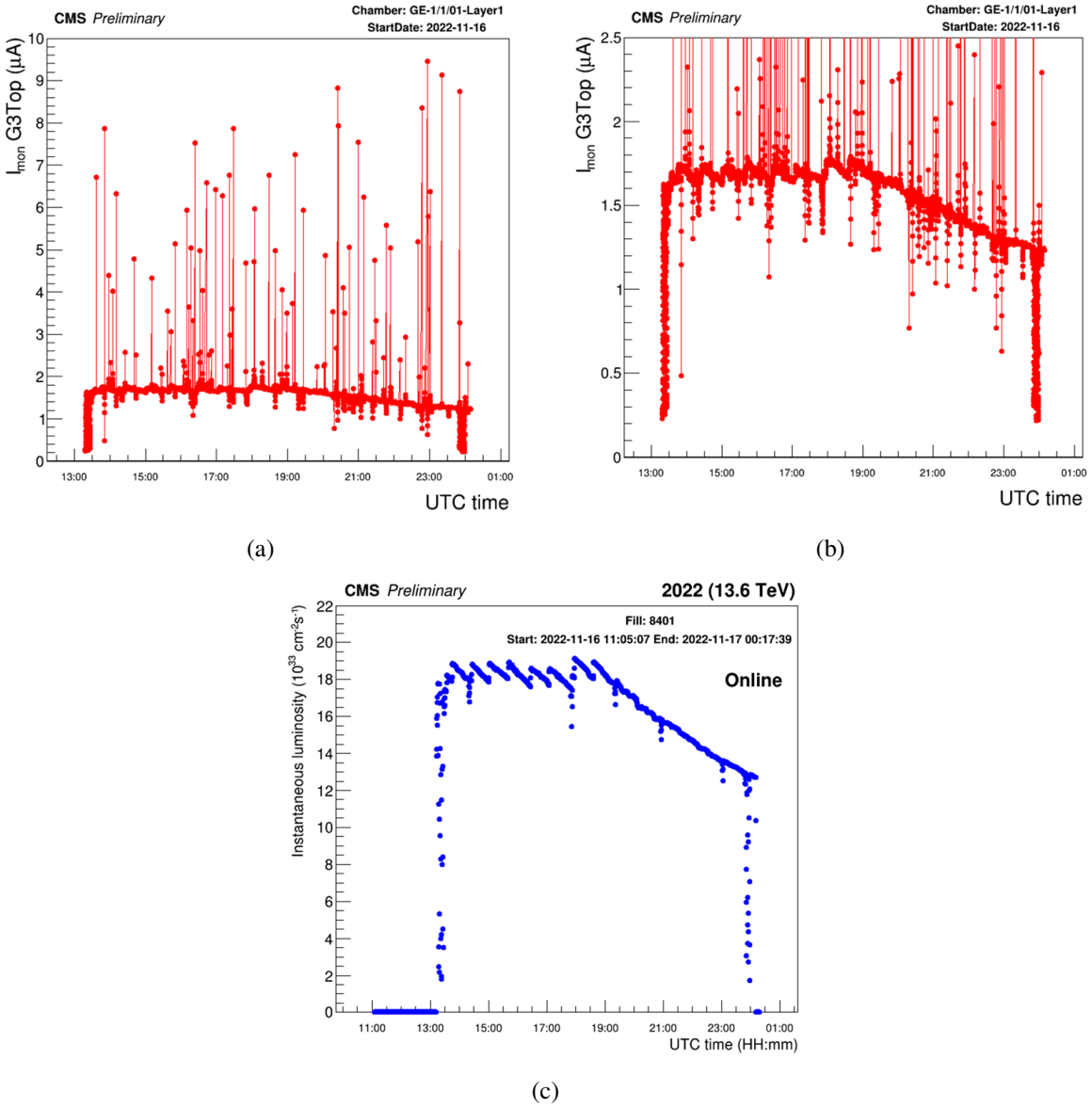

Figure 9. (a) Example currents observed on the G3Top electrode in presence of the stable collisions of 2450 proton bunches of the LHC beams in one GE1/1 module. The presence of discharges (current spikes), over a baseline current evolving in time, can be observed (b). The shape of the baseline current reflects the profile of instantaneous luminosity of the p-p beam collisions (c). Reproduced from [23]. The Author(s). CC BY 4.0.

The HV working point I_{eq} = 690 µA was maintained till the end of 2022 data taking, with a stable mean discharge rate of around 0.5-1 discharges per hour per single module.

From the 2022 data collection, we can derive several key points:

- the electrodes most prone to discharges are those that provide the potential difference responsible for generating the electric field inside the GEM foil holes — specifically, the Top channels of the A1515BTG board. This phenomenon can be clearly seen in figure 12, where the raw number of discharges are shown per each electrode as function of their amplitude.

2025 JINST 20 P05035

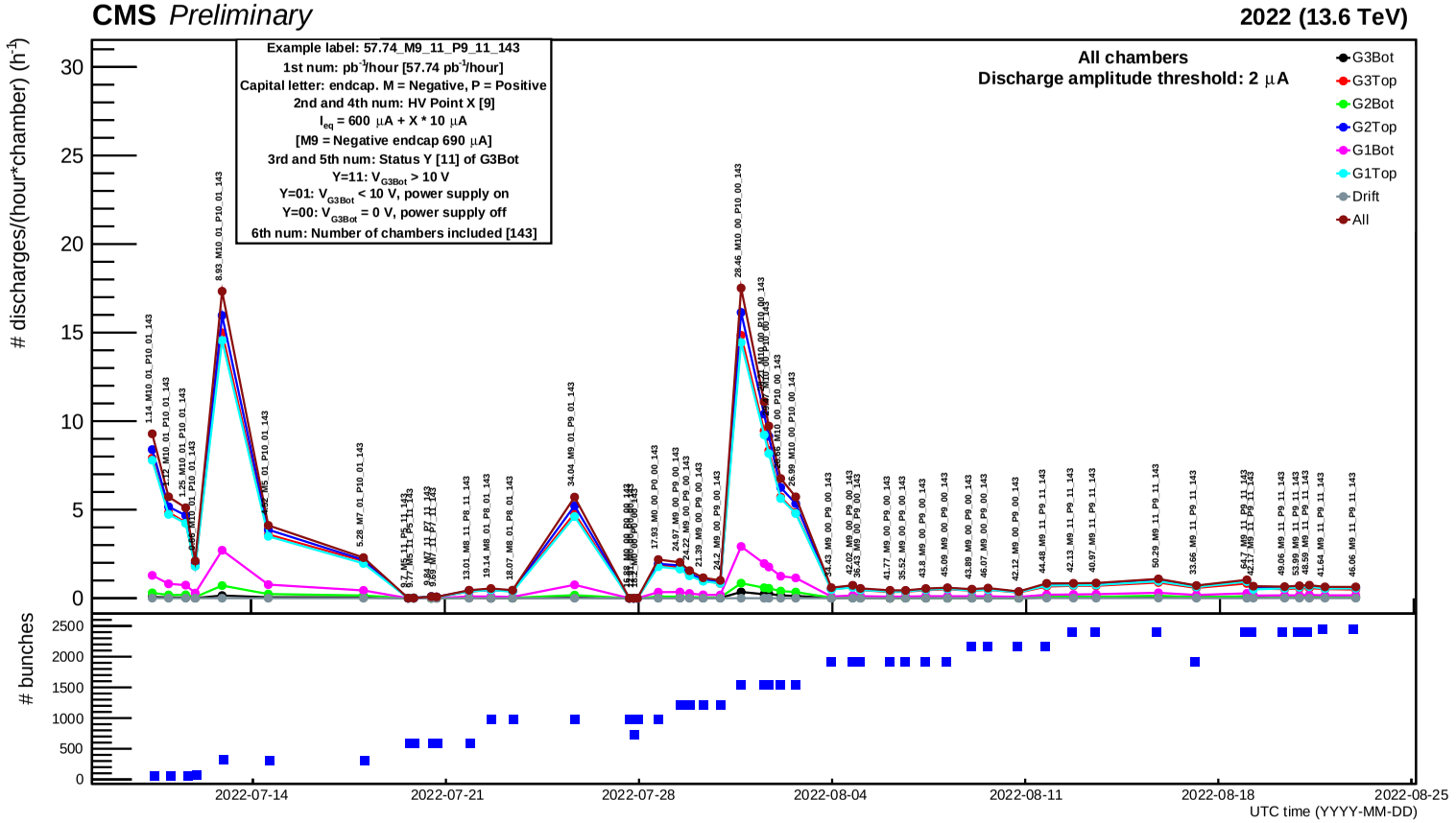

Figure 10. Average rate of discharges per hour per single chamber. The rate corresponding to each power supply channel is illustrated. In addition, the line called "All" is the logical OR of the discharges observed at the same timestamp for all the seven power supply channels that power a module. Each point has a label attached which provides information on the HV working point and on the rate of delivered luminosity per hour by the LHC. In the initial part of July the detectors were operated at I_{eq} = 700 µA. In the following weeks the working point was adjusted to decrease the discharge rate. At the end of July I_{eq} = 700 µA was applied again, corresponding to the highest discharge rate part at the center of the plot, decreasing in time during the following LHC fills, keeping G3Bot OFF to limit the energy involved in a discharge propagating towards the readout electronics. Then, I_{eq} = 690 µA was adopted, at first with G3Bot OFF, and at the end of August all the seven HV electrodes in the GEM stacks were powered, achieving a discharge rate of around one discharge per single chamber per hour. Reproduced from [23]. The Author(s). CC BY 4.0.

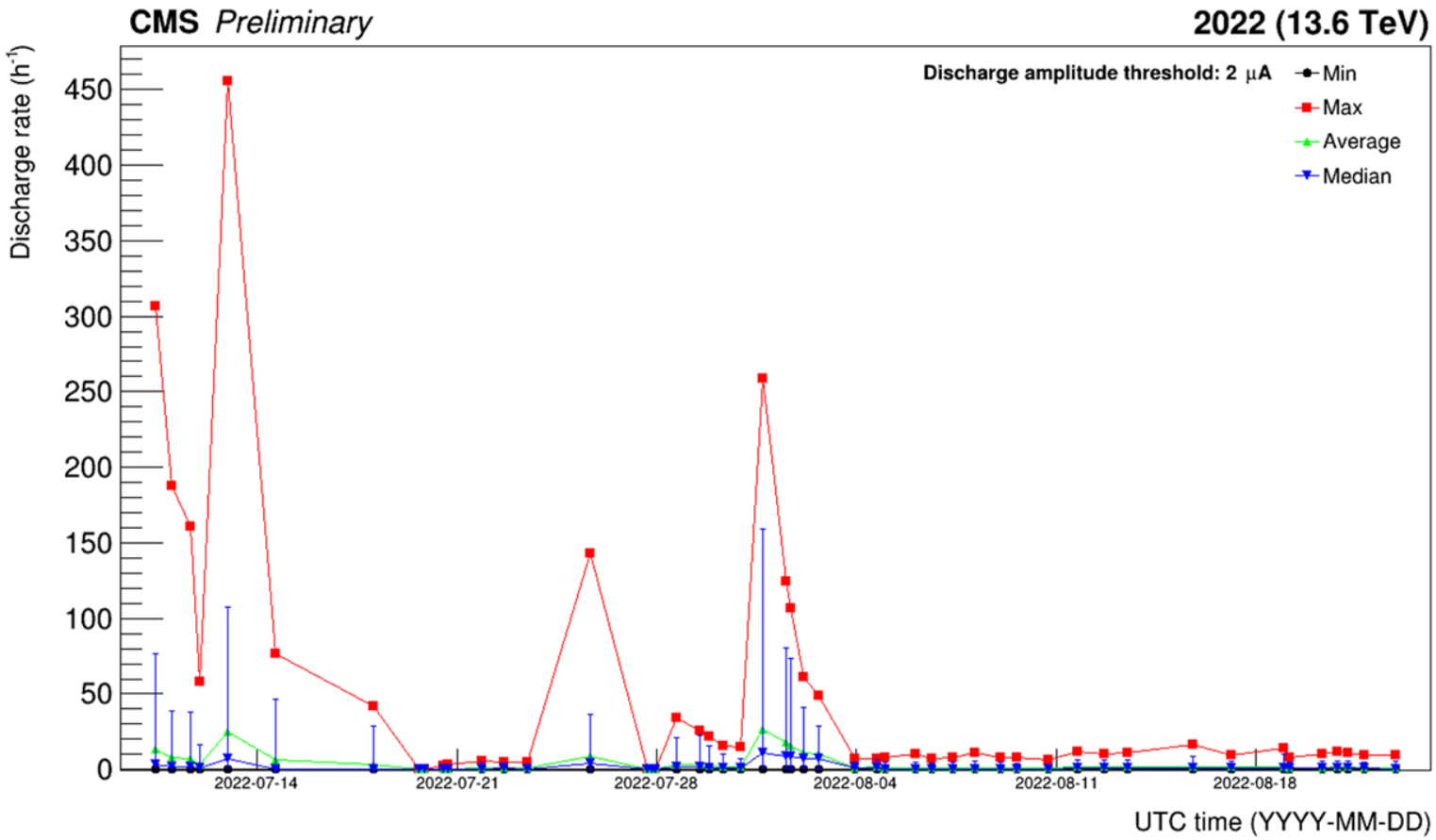

Figure 11. Main statistic indicators for the distribution of discharge rate observed per each independent HV power line used to power GE1/1 detectors. The dataset includes 72 values of discharge rate (one per HV power line), per each LHC fill analyzed. The results are displayed per pair of chambers because is not possible to disentangle which module within a pair generated a given discharge. In July and August 2022, there were 72 independent HV power lines, one per pair of chambers covering the same CMS ϕ sector (GE1/1 super-chamber). Therefore, the discharge rate per HV power line is the discharge rate per super-chamber. During this period one module in one single super-chamber was not connected to the HV. That is the only case where the discharge rate per power line is not that of the super-chamber. We chose to display the maximum, minimum, average and median discharge rate per HV power line among the 72 values per fill. The median error bar covers the data contained within two standard deviations, so from the quantile 0.02703 to the quantile 0.97296.

- The discharge rate decreased over time following the first irradiation period of the chambers, likely due to factors such as GEM foil conditioning and the removal of imperfections in the GEM holes. This trend is evident when comparing the first week of data-taking — when the chambers were operated at I_{eq} = 700 µA and experienced the highest number of discharges — with the period at the end of July, when the same HV working point was used. This comparison highlights how the discharge rate evolved under consistent operational conditions.

  This effect of decreasing discharge rate at a fixed HV working point can better be observed from the decreasing trend of the maximum discharge rate at the center of figure 11 (between the 31st of July and 2nd of August), and the same trend is also followed by the median. This is in part due to the effect of repeated occurrence of discharges in the same chambers, which in time removed the imperfections in GEM holes. On the other hand, the occurrence of discharges can lead to the generation of short circuits, which in turn can result in a reduction of the discharge rate due to the lower voltage effectively applied to the GEM foil. Nevertheless, only one chamber developed a permanent short circuit during the second period with I_{eq} = 700 µA, also maintaining the same discharge rate (∼ two discharges per hour). Therefore, the main contribution to the reduction in the discharge rate over this period was due to the conditioning of the foils. Indeed, the difference in the mean luminosity delivered by the LHC is only approximately 5%, which is not compatible with the observed difference in the discharge rate, as can be seen in figure 10 between the 31st of July and 2nd of August.

- Finally, the mean discharge rate per super-chamber with G3Bot ON at I_{eq} = 690 µA is around two times higher than the one observed with the G3Bot OFF at the same HV working point, as reported in table 5.

Table 5. Comparison of discharge rate between G3Bot OFF and G3Bot ON, with HV working point I_{eq} = 690 µA. The lower threshold on the discharge amplitude, to count a discharge, is 2 µA.

G3Bot status	Average LHC delivered luminosity per hour (pb^{-1}/hour)	Discharge per LHC delivered luminosity per Super-Chamber (events/pb^{-1})	Discharge per hour per Super-Chamber (events/hour)
OFF	42.1	$(1.8 \pm 0.3) \cdot 10^{-2}$	0.8 ± 0.1
ON	44.5	$(3.8 \pm 0.5) \cdot 10^{-2}$	1.7 ± 0.2

In conclusion, the generation of several short circuits in GEM foils was observed during the data taking. Their evolution in time is illustrated in figure 13. The most significant period for their generation is represented by the first months of the year, where detector and magnet commissioning activities are performed. The context of generation and healing of short circuits will be analyzed more deeply in section 4. The term "healing" for a short circuit is the process by which a short circuit in the GEM detector resolves itself, restoring the normal function of the affected HV sector or detector.

3.3 Second year of Run-3 operations with beam

During the second year of Run-3 (2023), the detectors were operated at a globally lower HV working point, with respect to the previous year. In addition, the individual chambers working points were

2025 JINST 20 P05035

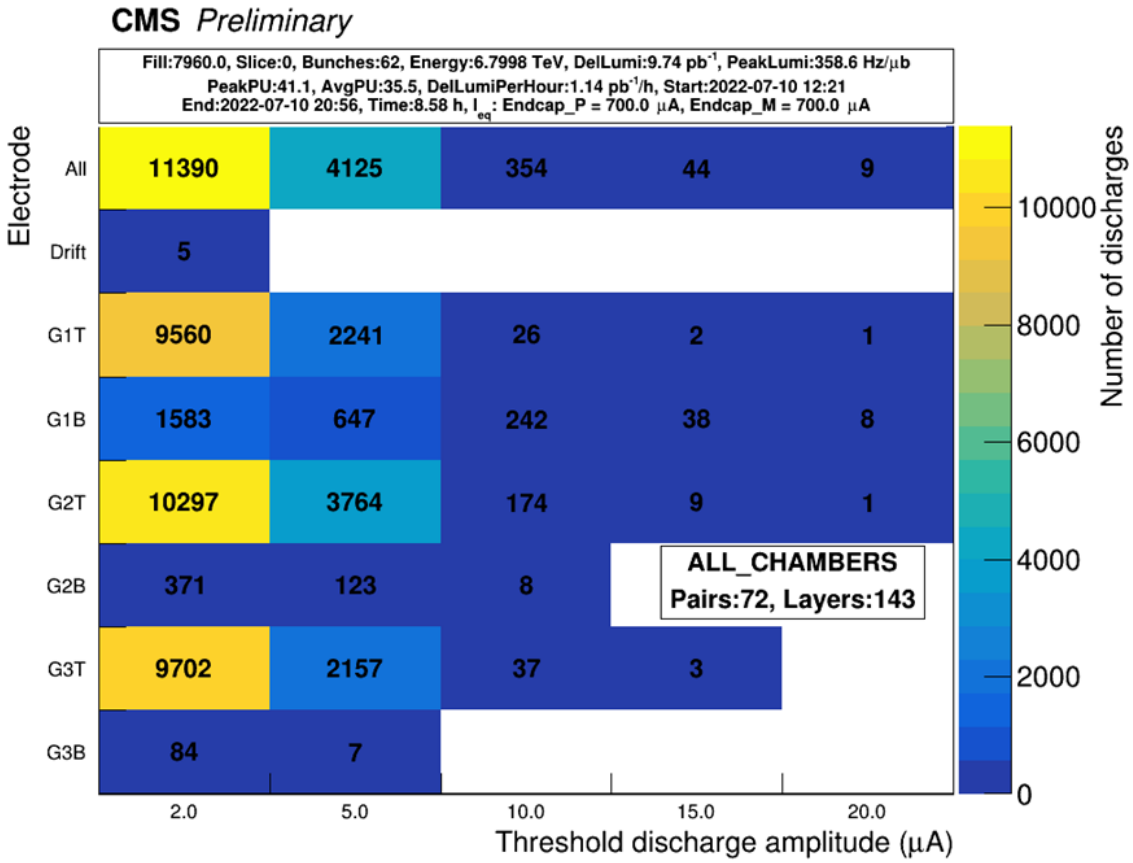

Figure 12. Example of the raw number of discharges observed during an LHC fill, on each electrode powering 143 GE1/1 detectors installed in CMS, as a function of their amplitude. On top of the plot, the information describing the LHC fill parameters and the global HV configuration of the two endcaps is shown. In the bottom right side is reported the number of single chambers powered by HV (*Layers*) and the number of independent HV lines (*Pairs*). The number of independent HV lines was still 72. A total of 143 modules were connected to the HV system and only one was disconnected, due to an issue on one of its HV filters. The label "All" on the first line of the plot indicates the logical OR between the different seven electrodes, to have a global number of discharges in the fill, without double counting. Reproduced from [23]. The Author(s). CC BY 4.0.

adjusted, depending on the needs of the single modules in terms of efficiency. In general the HV working points used during 2023 were $I_{\text{eq}} = 670\,\mu\text{A}$, $675\,\mu\text{A}$ and $680\,\mu\text{A}$. During p-p collisions, an average discharge rate $R < 0.1\,\text{discharges}/(\text{hour} \cdot \text{chamber})$ was observed.

Finally, in 2023 the LHC produced the first Run-3 collisions of lead-lead ions (Pb-Pb). In this case the instantaneous luminosity of colliding LHC beams $O(10^{27})\,\text{cm}^{-2}\text{s}^{-1}$ is around 7 orders of magnitude lower than the instantaneous luminosity during p-p collisions, $O(10^{34})\,\text{cm}^{-2}\text{s}^{-1}$. As a result, only a few units of discharges were observed per LHC fill. The HV data analyzed covered $2005.7\,\mu\text{b}^{-1}$ of luminosity delivered by the LHC, with a medium number of discharges counted in the whole system per fill around 5.9 ± 0.7. Throughout the entire Pb-Pb collision period, the number of discharges counted by the whole GE1/1 station was always lower than 30 discharges per fill. The same HV working point adopted in the previous months for p-p collisions was used also for the Pb-Pb period. The numbers corresponding to the observation done in this period are summarized in table 6.

2025 JINST 20 P05035

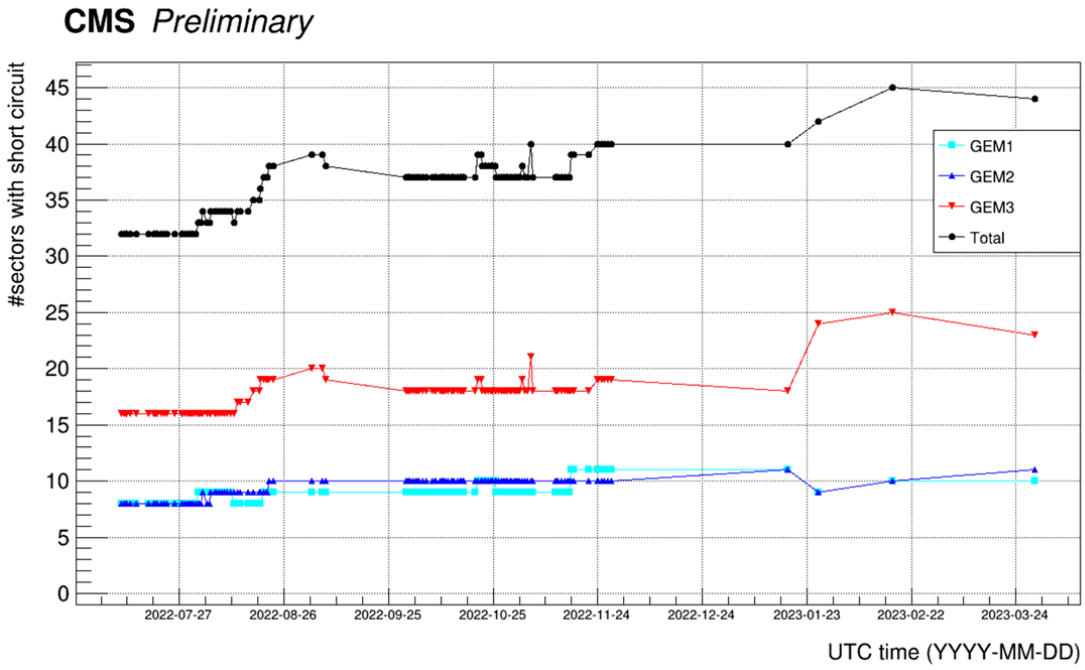

Figure 13. Evolution in the number of HV sectors affected by a short circuit in GE1/1 detectors during 2022 data-taking period (July-November) and during the detector commissioning activities in the first month of 2023. The total number of HV sectors in the GEM foils in the whole GE1/1 station is 18792, with 40 (47) HV sectors in each of the three foils of the 72 short (long) modules. Reproduced from [23]. The Author(s). CC BY 4.0.

Table 6. The table summarizes some numbers for the operations with Pb-Pb collisions, respectively concerning the discharges and the LHC delivered luminosity observed. The number of discharges shows the average counts per fill generated by all the 143 GE1/1 detectors and the total summing the contribution of all analyzed Pb-Pb fills. Similarly, the second line shows the luminosity delivered by the LHC per fill and the total integrated over all Pb-Pb analyzed fills.

Quantity	Average per fill	Total
Discharges (143 chambers)	5.9 ± 0.7	347
Delivered luminosity	$34.0 \pm 2.7\,\mu b^{-1}$	$2005.7\,\mu b^{-1}$

This last part of 2023 data-taking confirmed the observation of a correlation between the instantaneous luminosity and the discharge rate. The correlation between the two quantities is under study. For physical reasons, such a correlation is expected: a higher number of ionizing particles creates a more demanding operational environment for the detectors, making them more susceptible to discharges. A thorough study is needed to understand if the correlation is due only to this aspect or some other phenomena play a role.

4 Generation and healing of short circuits in GEM foils

In this section, we will summarize the observations accumulated during the first years of operation of the GE1/1 detectors in CMS, until 2023. The focus will be on the generation and healing

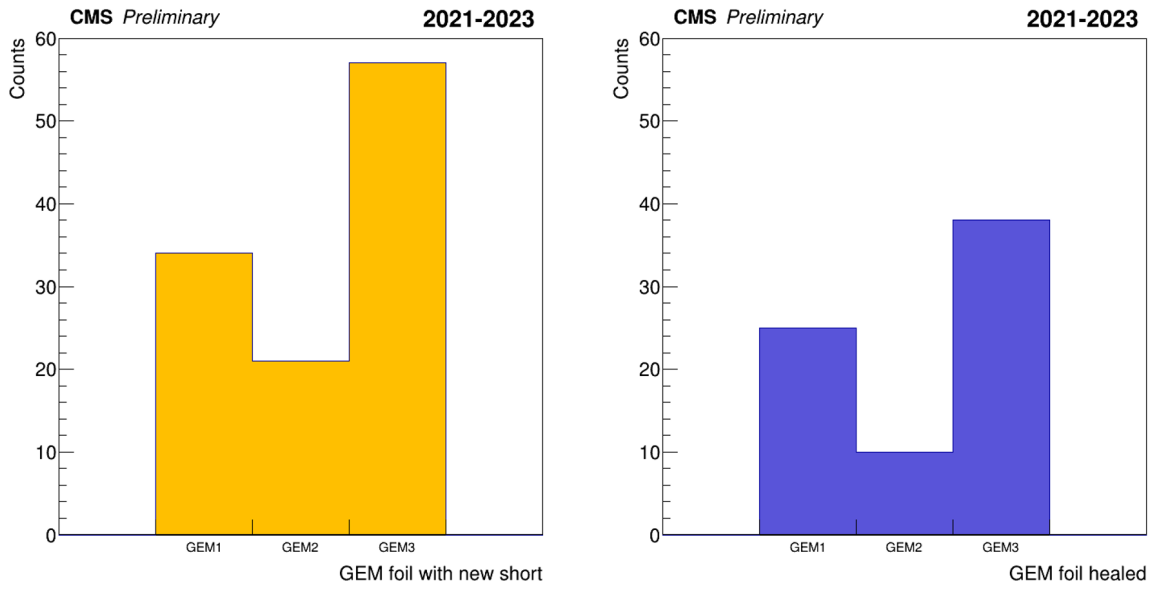

Figure 14. Number of times a given GEM foil is involved in a generation or healing event of a short circuit. The plot shows that the GEM3 foil is involved in the generation of short circuits in a number cases around two times higher than the other two GEM foils.

of short circuits. The origin of these phenomena is already treated in [25, 26], where it can be inferred that one of the probable causes of the generation of short circuits is the presence of dust inside the chamber.

From previous observations, a correlation between the presence of the magnetic field and the generation of short circuits has been observed, and in the following a more detailed study of the behavior of the chamber under the influence of the CMS magnetic field [27] is presented. Then, the correlation with the applied HV and the gas mixture is studied.

In order to determine the circumstances surrounding the generation or healing of the short circuit, we considered the data related to the chamber's operational conditions, including the gas-mixture utilized, the HV working point, the presence of discharges, and the voltage ramp up of the affected electrode and the whole chamber. Additionally, the status of CMS at the same timestamp of short circuit generation or healing is investigated, taking into account the presence of the LHC beam and the magnet operations.

As a preliminary observation, the generation and healing of short circuits have been noted, as illustrated in figure 14. The number of short circuits generated and healed is obtained by examining the behavior of the currents in each HV power line, as detailed in section 2.3. The plot shows that GEM3 foil is involved in the generation of short circuits with a factor of two higher with respect to GEM1 and GEM2, shown also in figure 13. The reason behind this observation could be explained by looking at the triple-GEM structure, where the GEM3 foil represents the final stage in the avalanche multiplication and thus the stage that collects the highest amount of charge among the three amplification stages of the primary ionization charge. In addition, the observations indicated that the majority of the events resulted in the generation or healing of a single HV sector at a specific point in time, as can be seen in figure 15.

2025 JINST 20 P05035

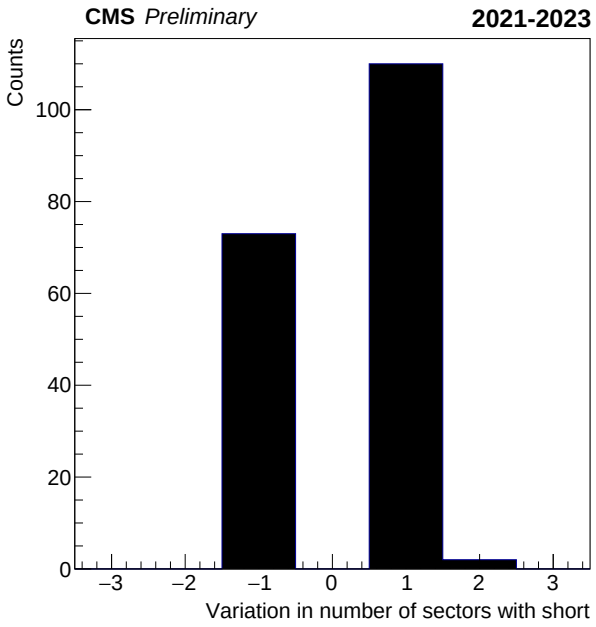

Figure 15. Variation in number of HV sectors affected by a short circuit at a given instant, in the whole GE1/1 system (both long and short chambers). A positive number means a generation of a new short circuit, while a negative number flags a healing. In one single occasion it was observed the healing of one HV sector in two distinct foils in the same module at the same timestamp. Because it affected two different foils, this event is represented as two distinct healing events (two entries for −1 in the plot).

4.1 Role of the magnetic field

A particular role in the generation of short circuits is played by a variation of magnetic field during a CMS magnet ramp. The generation of short circuits appears to be independent of both the magnetic field strength and the direction of the ramp (up or down), as shown in figure 16. However, the distribution shows a slight excess of short circuits during magnet ramp down compared to ramp up. This is attributed to the contribution of the initial magnet ramp down in November 2021, which occurred when HV was OFF and a procedure to handle HV during magnet ramps had not yet been developed, more detailed in section 5.1. Indeed, during the aforementioned magnet ramp down with HV OFF, six short circuits were generated. Upon subtraction of the contribution of short circuits generated in 2021 related to magnet operations (two during magnet ramp up, seven during magnet ramp down), a slight preference for short circuit generation in case of magnet ramp down becomes evident. There are three counts for magnet ramp up compared to nine events for magnet ramp down. These observations do not provide sufficient evidence to conclude that magnet ramp down is preferentially associated with the generation or healing of short circuits, given the limited statistical sample size. The sample on which the analysis is based will be expanded in the near future to take advantage of the remaining years of Run-3 data collection.

To face the instability due to discharges during magnet operations and, with a higher relevance, the short circuit generations in the same operating conditions, in December 2021 the first tests to develop a safe procedure for HV operation during magnet ramps were conducted. Those tests took place in the CERN North Area using the Goliath magnet and the results are presented in [26].

2025 JINST 20 P05035

The observations accumulated from 2021 to 2023 operations showed that the events of generation or healing of short circuits occur at the beginning or at the end of a magnet ramp, predominantly at 0 T or 3.8 T, as shown in figure 17. The histograms exclude all events that occurred while the magnetic field was stable, as well as events where the HV was OFF during a magnet ramp. In this second case, short circuit generation is observed after the magnet ramp has already finished. As a result, an incorrect magnetic field value would be assigned, even if the magnet ramp was responsible for its generation or healing. No healing events were observed after a magnet ramp was performed with HV OFF.

Magnetic field variations during CMS magnet ramps play a role in the generation and healing of short circuits, predominantly during the transitions at the start and at the end of the ramps. In particular the short circuit generation during magnet operations is only observed when the magnetic field approaches 0 T, while the healing is observed when the field is close to 0 T or 3.8 T. These observations suggest a dynamic response to ramping conditions, but further study is required to identify the precise physical mechanisms and confirm the correlation.

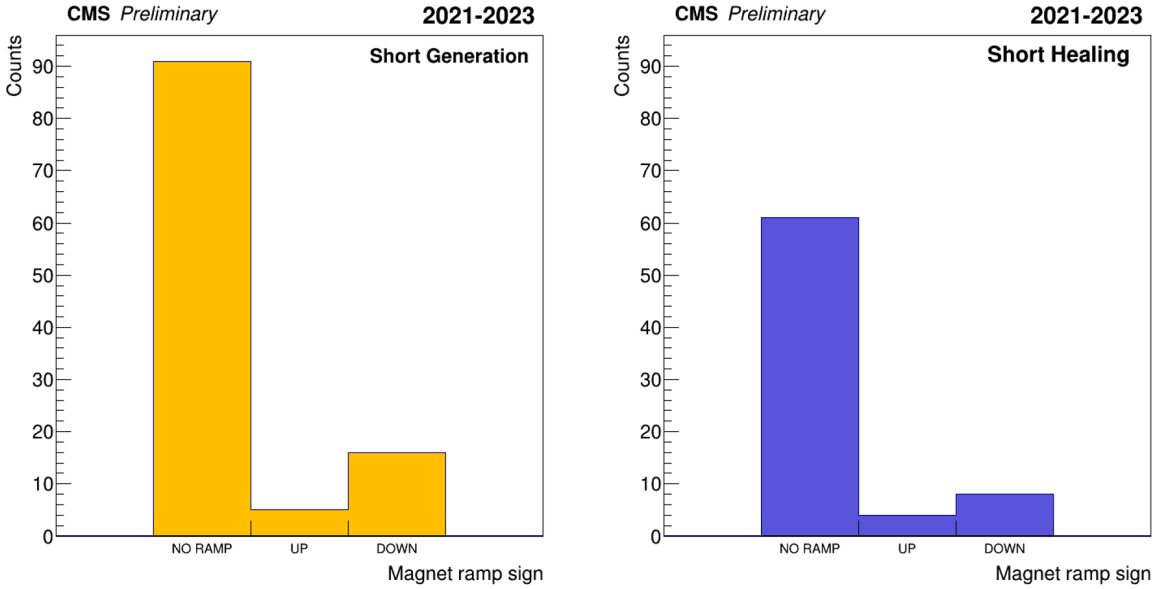

Figure 16. Sign of magnet ramp involved in the generation or healing of short circuits in GEM foils. The plot shows no preference on the sign of the magnetic field ramp for the generation and healing of short circuits in GEM foils. The contribution to the excess in the generation of short circuits during ramp down, respect to ramp up, is due to the contribution of the first magnet ramp down in November 2021, when no protective measurement was yet implemented.

4.2 Role of the HV working point

Another important parameter to monitor is the HV working point. Figure 18 shows the value of HV applied, during a magnet ramp, to the GEM foil affected by generation or healing of a short circuit. This plot confirms that keeping HV OFF during a magnet ramp shows a higher number of short circuit generations.

In addition, figure 19 shows more in general the HV working point present at the time of generation or healing of a short circuit for each event observed in these three years. The values between 300 – 400 V include the voltages applied during the normal operation for data taking, adopting the

2025 JINST 20 P05035

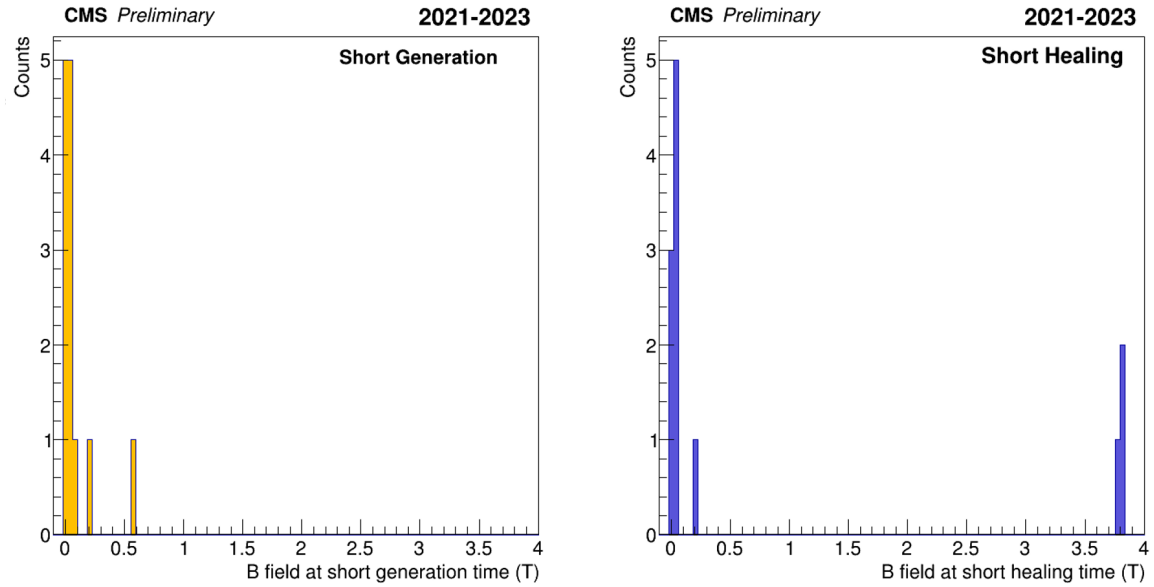

Figure 17. Value of magnetic field at which the generation or healing of a short circuit was observed in presence of a magnet ramp. The histograms exclude all the events occurred with magnetic field stable and the events where HV was OFF during a magnet ramp.

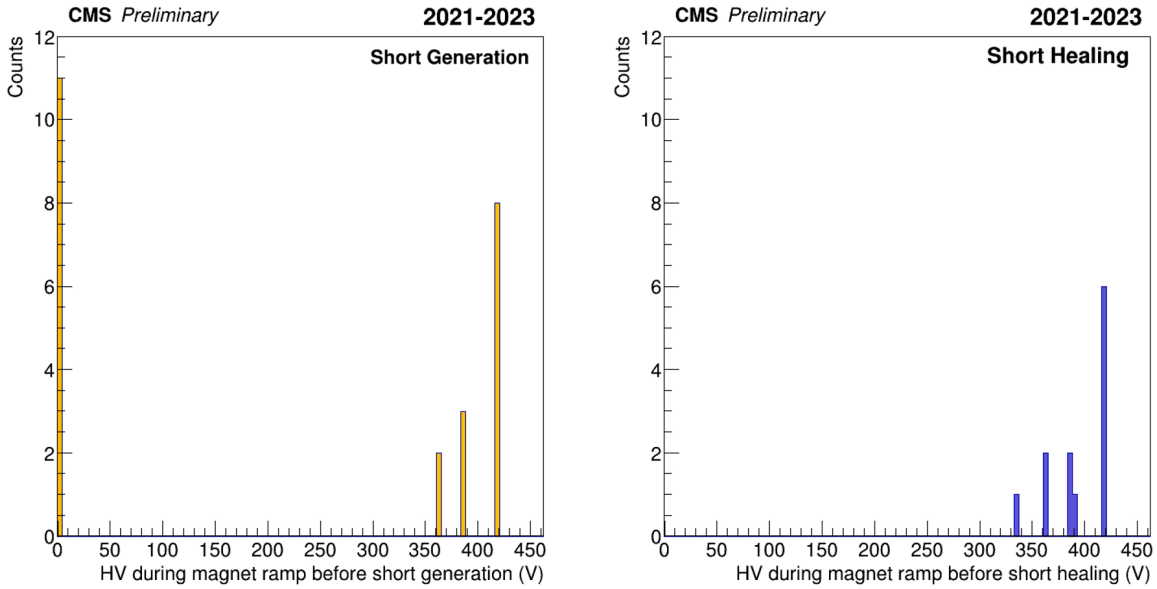

Figure 18. HV applied to a GEM foil during a magnet ramp, before the generation or healing of a short circuit. In this plot is shown a significant contribution to the generation of short circuits in the case of chambers kept with HV OFF during the magnet ramp.

working points illustrated in table 3 up to $I_{eq} = 700\,\mu A$. Otherwise, the values with HV ≥ 430 V are applied during the restart of the operations at the beginning of the year, when the detector is operated in pure CO_2 and in the first phases of operations in Ar/CO_2 (70/30).

2025 JINST 20 P05035

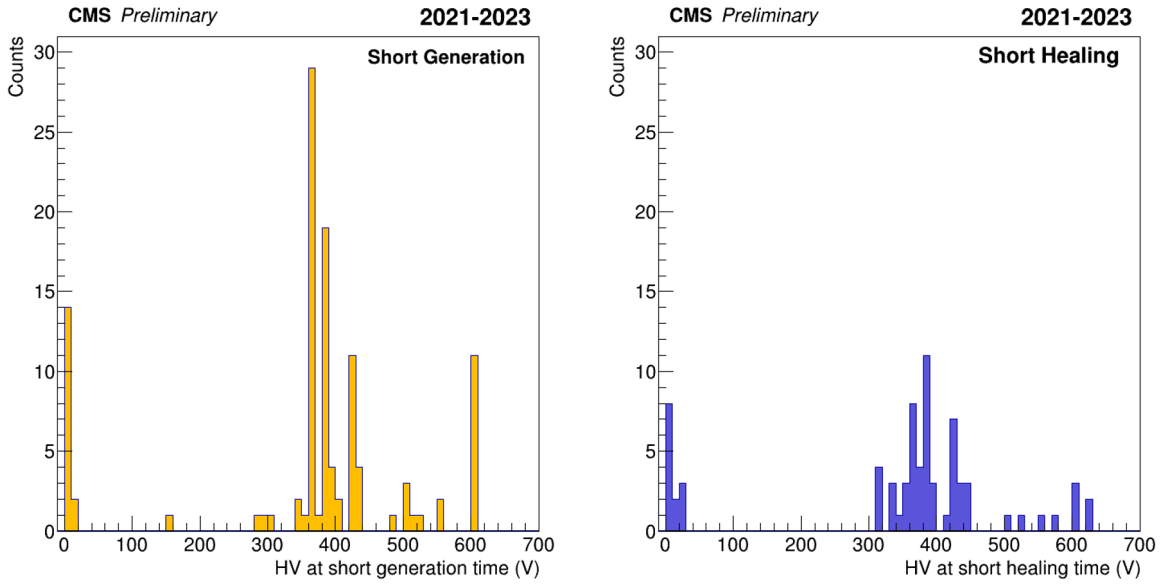

Figure 19. HV applied to a GEM foil at the time of generation or healing of a short circuit, for each event observed in three years of operations (2021-2023). In order to check the presence of a short circuit, it is necessary to turn ON the HV. Consequently, a number of short circuits were identified as either newly generated or undergoing healing during the HV power up of the chamber.

4.3 Role of the gas mixture

The gas mixture present at the moment of the short circuit generation or healing was also investigated as partly anticipated in the previous subsection, and the results are reported in figure 20. The number of short circuits generated or healed was normalized by the amount of time that each gas mixture was used over the three-year period between 2021 and 2023. Specifically, the chambers were operated in pure CO_2 for 159 days and in Ar/CO_2 (70/30) for 834 days. Furthermore, in 2021, the chambers were operated for 41 days in Ar/CO_2 (50/50), and no variation in the number of short circuits was observed with this configuration.

It can be seen that the healing process does not show a particular preference for a specific gas mixture. On the other hand, it is clear that most of the short circuits are generated in the period where pure CO_2 is used. This does not imply that the responsible of this effect is only the gas, since the two gas mixtures correspond to two distinct types of activities. In particular, the period during which pure CO_2 is applied corresponds with the first restart after the end of year power OFF of the detectors. Moreover, in the same period higher HV working points are used, exceeding HV $\geq$ 430 V. This conclusion is confirmed by the combination of HV working point and gas mixture normalized by days of usage in figure 21.

From the plots cited above, it appears clear that short generation has no significant dependence on the gas mixture but is instead influenced by the HV working point. Indeed, from the CO_2 column we can observe that the two bins with the highest number of short circuits normalized per day of gas mixture, correspond to the highest HV working point value and to the OFF value.

4.4 Context of short circuit generation

It was observed that the context of generation and healing of short circuits can involve several processes. We summarize the mechanisms in figure 22. The processes that are frequently involved

2025 JINST 20 P05035

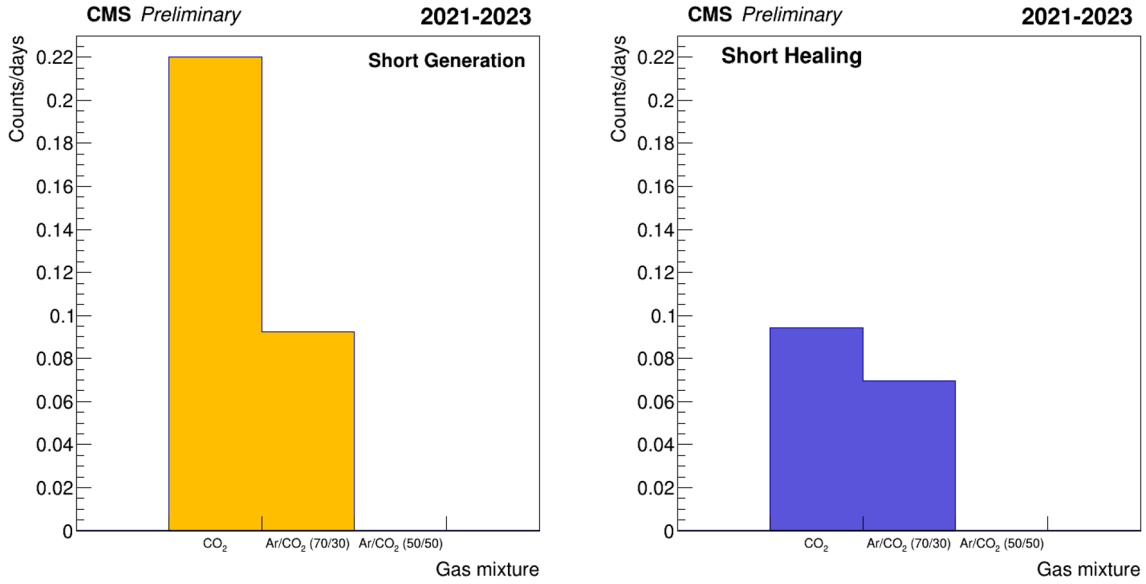

Figure 20. Number of short circuits generated or healed per day of application of a given gas mixture. In the specific, in these three years the detectors were operated in pure CO_2 for 159 days, in Ar/CO_2 (70/30) for 834 days. Moreover, in 2021 they were operated for 41 days in Ar/CO_2 (50/50) and no variation in the number of short circuits was observed in those days.

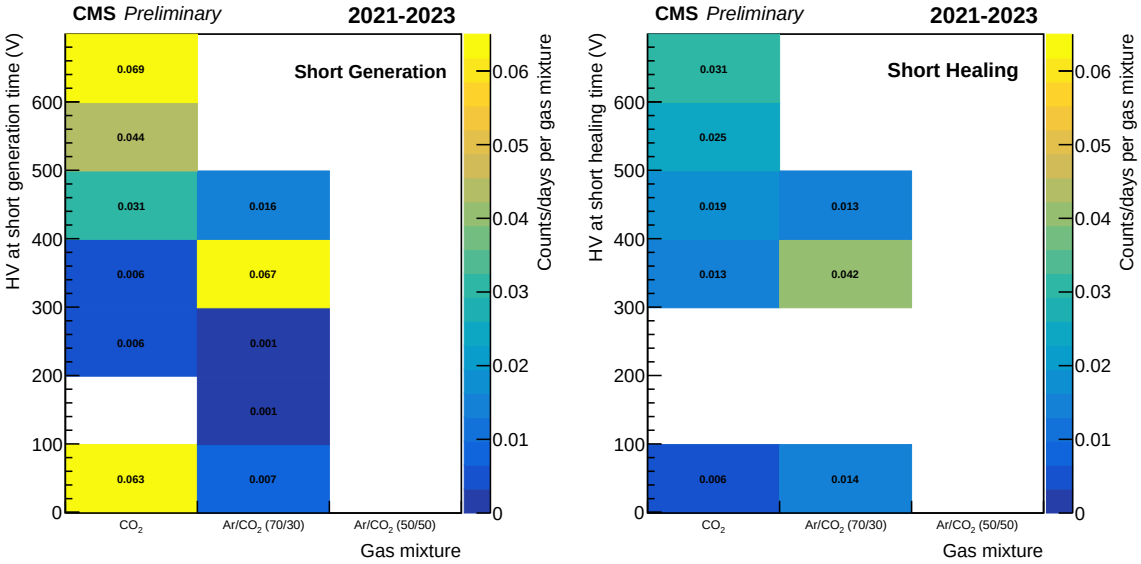

Figure 21. Number of short circuits generated or healed per day of application of a given gas mixture and HV applied. The most populated bins for the generation of short circuits, in presence of pure CO_2 gas mixture, are the one with the highest voltage applied and the one corresponding to the OFF value. In the column corresponding to the Ar/CO_2 (70/30) gas mixture, both for short generation and healing, the most populated bin is the one with the voltage applied between 300 V and 400 V, which is the range used for the normal data taking.

in the generation and healing of short circuits include the occurrence of discharges, magnet ramps, and variations of voltage that are applied to the chamber.

2025 JINST 20 P05035

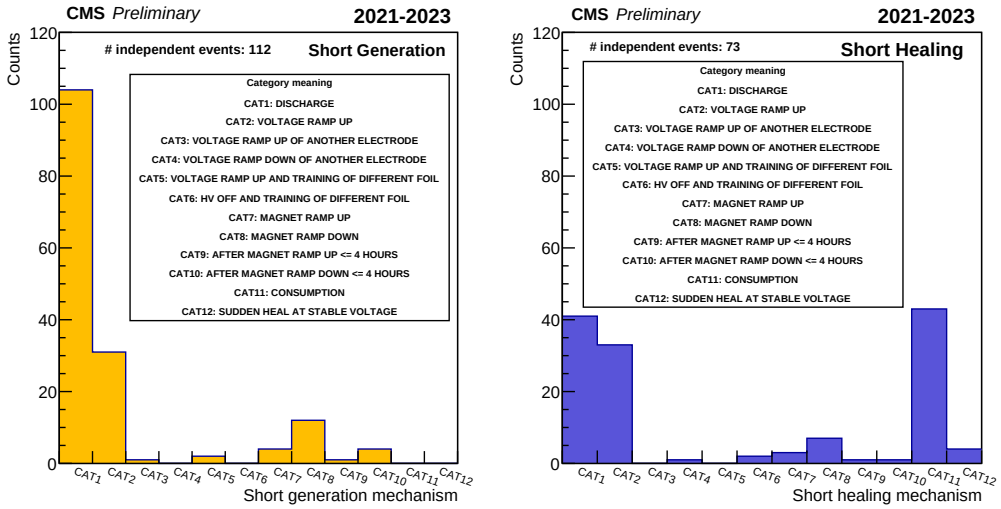

Figure 22. Mechanisms involved in a generation or healing event of a short circuit. More than one mechanism can be involved in the same event (for example if a discharge and a magnet ramp up are involved in an event, this will be counted in both categories bins).Reproduced with permission from [28].

The healing of many short circuits is attributed to a gradual reduction in the current drained by the short circuit, which is a consequence of the short circuit itself being gradually consumed. We refer to this phenomenon as "consumption" of the short circuit, which results in a gradual increase in the resistance of the connection. Figure 23 illustrates an example of this process, which appears to be a consequence of the burning or consumption, by different chemical processes, of the electrical contact responsible for the short circuit. This phenomenon may be attributed to the presence of chemical residuals within the chambers.

As the phenomenon was observed on multiple occasions, it is valuable to present the first observations. Figure 24 illustrates the sequence of events that initiated the observed consumption. The primary causes identified are delineated in the plot, including voltage ramp up, discharge, healing of another short circuit, magnet ramp down, magnet ramp up, and stable voltage. Each event can be triggered by one or more ignition processes. In total, 43 independent events were observed. Furthermore, the time elapsed between the generation of the short circuit and the start of its consumption is indicated on the x-axis. From the plot, it can be observed that the majority of short circuits that healed by consumption involved the occurrence of a discharge and a voltage ramp-up. The second valuable insight into this process is presented in figure 25, which illustrates the time in days needed for a short circuit to heal completely, from the start of the consumption process.

4.5 Summary on short circuit observations

To conclude this section, we present the operational periods during which the short circuits were generated. For the GE1/1 detectors, four main operational periods can be identified:

- OP1: the restart at the beginning of the year after the technical stop, during which the detector is OFF. The temporal extent of this interval is up to and excluding the initial magnet ramp of the year;
- OP2: all the operations performed in absence of stable beam;

2025 JINST 20 P05035

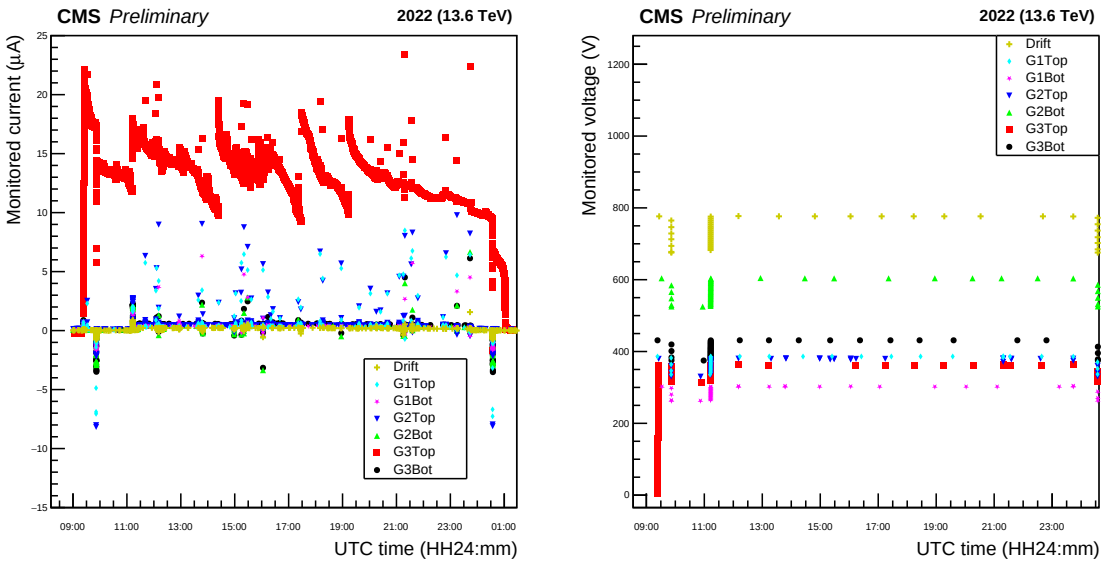

Figure 23. Example of a short circuit which slowly heals, decreasing gradually the current drained from the power supply, to finally heal. We refer to this process as healing by short circuit consumption.

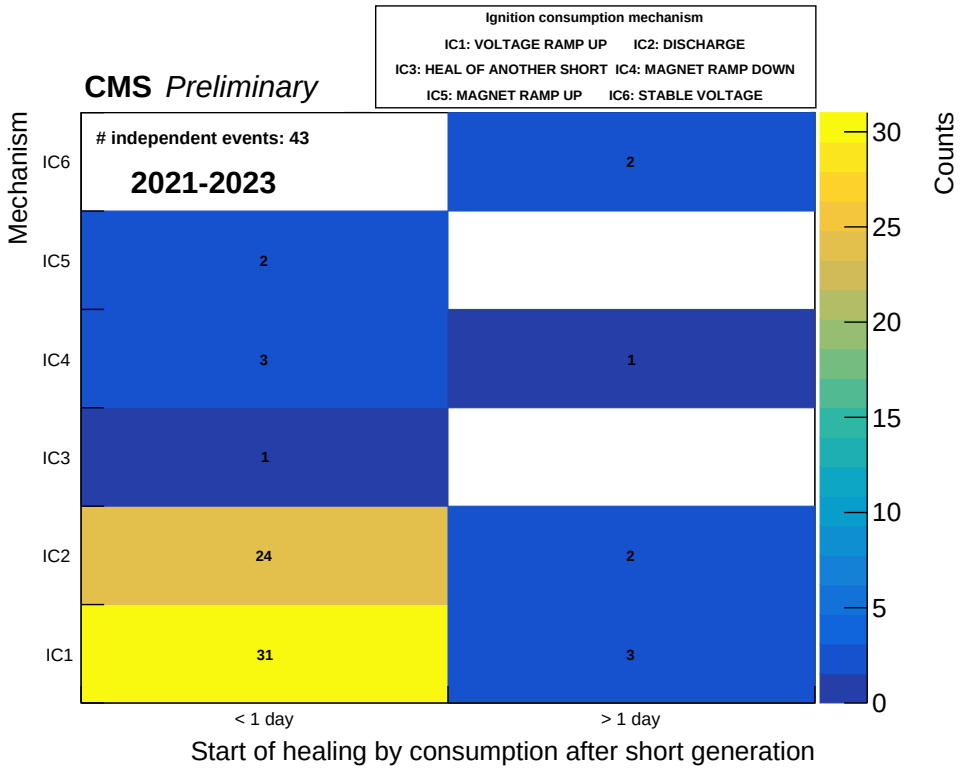

Figure 24. The plot shows on the X-axis the time that elapsed between the generation of the short circuit to the start of the healing by consumption, while on the Y-axis the mechanism that ignited the healing. More than one category can be involved in the ignition for the same healing event. The plot includes only the events of short circuit healing (2021–2023) that healed by gradual consumption of the short circuit, for a total of 43 "# independent events".

2025 JINST 20 P05035

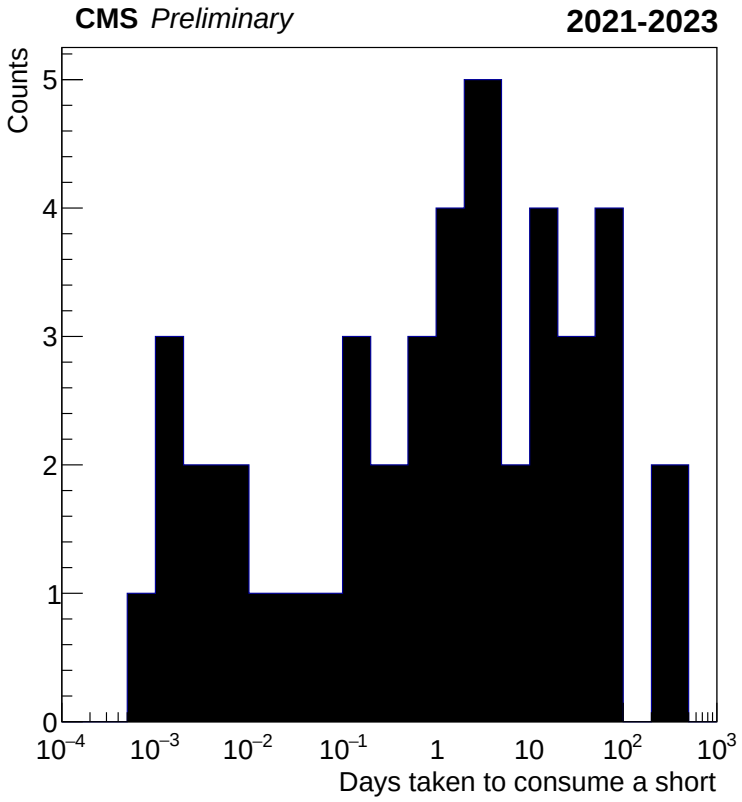

Figure 25. Time needed for a short circuit to heal by consumption (gradual decrease of the current drained by the short circuit). The plot includes only the events of short circuit healing (2021-2023) that healed by gradual consumption of the short circuit.

- OP3: the magnet ramps and the HV training performed immediately after them;
- OP4: the operation of the detector in presence of LHC stable beams.

Figure 26 summarizes the short circuits generated and healed over the three operation years, while figure 27 shows the contribution of each year. It is clearly visible that the main operation period contributing to the generation of short circuits is the restart of the year, after a period where HV was OFF for several weeks. During the same period, the HV training procedure is performed, with voltages above 430 V applied on the foils. These observations, together with the results shown in figure 19 suggest avoiding operation of the detector at excessively high HV values, such as 600 V and keeping the HV ON as much as possible to minimize the need for retraining the detector.

Figure 27 shows that the contribution of OP4 decreased from 2022 to 2023. One important research for this is that in the second year of Run-3, a lower HV working point was adopted, tuned for chambers individually between I_{eq} = 670 µA and I_{eq} = 680 µA, while in 2022 GE1/1 detectors were operated with an HV working point uniform for all chambers, in a range between I_{eq} = 690 µA (72% of 2022 LHC fills) and I_{eq} = 700 µA (10% of 2022 LHC fills). During the rest of 2022, a lower working point was used due to the tuning of the HV in the monitoring phase of the discharge rate.

2025 JINST 20 P05035

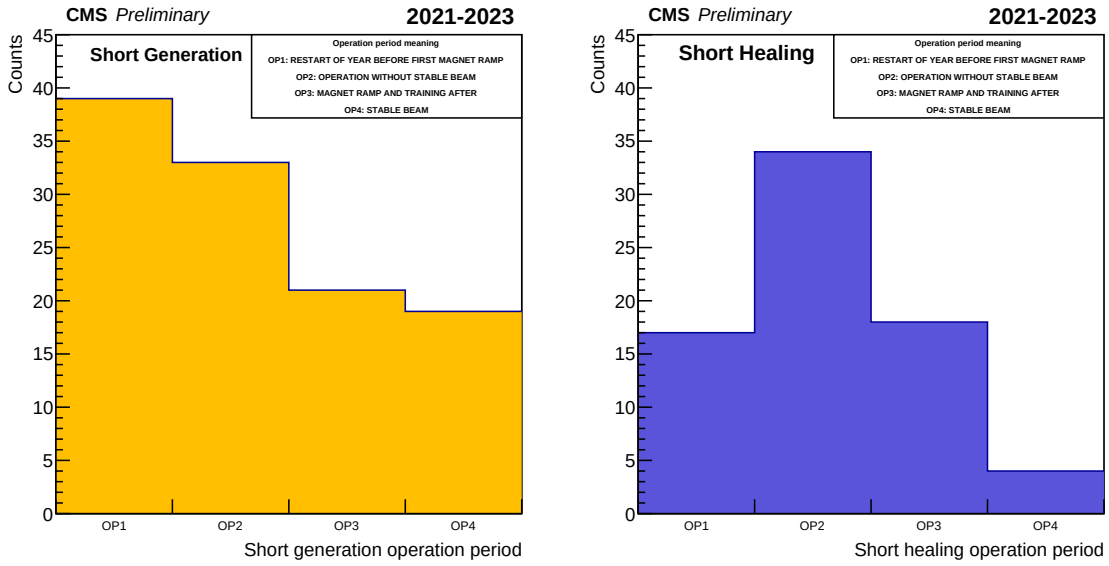

Figure 26. Operation period during which each short circuit was generated or healed, from 2021 to 2023. The plot shows that the highest part of the short circuit generation happens during the operations performed to recover the detector after a long period when it is kept with HV OFF at the end of the year.

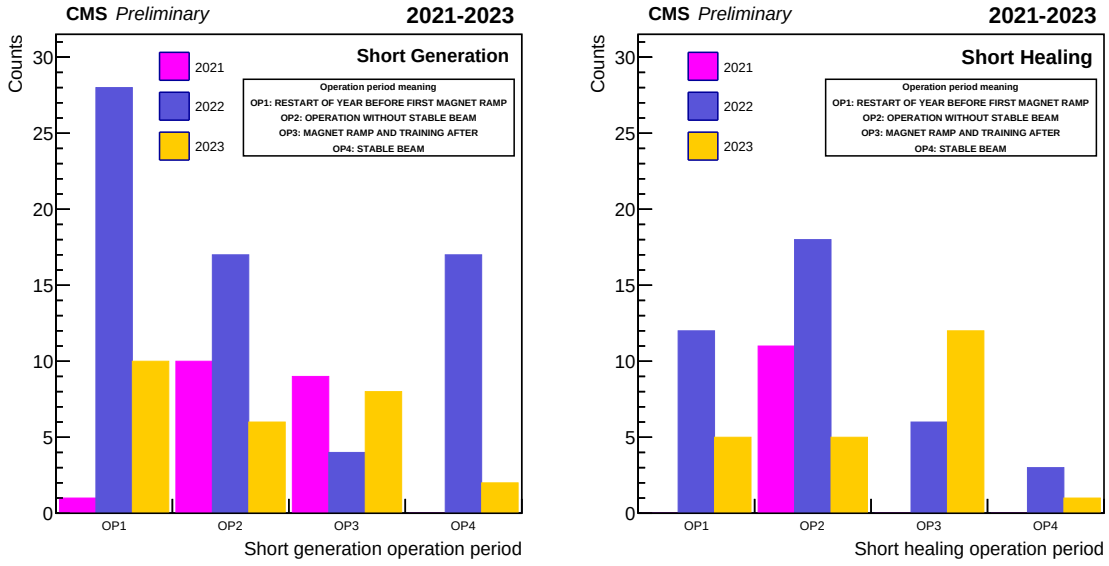

Figure 27. Operation period during which each short circuit was generated or healed by year. The plot shows as the year contributing more to the short circuit generation was 2022, in particular for OP4, because 2022 was the first year of operation of GE1/1 in presence of p-p collisions. On the other hand, 2022 is also the year with the lowest amount of short circuit generations due to magnet operations (OP3), because a lower number of ramps was performed in this year, as specified in table 7.

2025 JINST 20 P05035

5 Mitigation strategies

Several actions have been taken on the operation side to face the occurrence of short circuits, of discharges and to adjust the efficiency of the different chambers to achieve the highest possible value, while maintaining a low discharge rate. These include adjusting the HV working point, the implementation of a protection from magnet operation, and the HV re-mapping. They will be detailed in this section.

5.1 Implementation of magnet protection

In order to manage the occurrence of short circuits in case of magnet ramp, a protection was implemented in the GEM DCS. This protection gets automatically triggered every time the CMS magnet is declared as not stable, when the magnet current starts to vary in case of a ramp (both in case of ramp up or ramp down). As mentioned in section 4, the definition of the parameters of this protection were provided from the studies performed in 2021, when four GE1/1 chambers were tested in the magnetic field generated by the Goliath Magnet in CERN North Area. The results of these tests are illustrated in detail in [26]. The protection powers the detectors in the following way:

- voltage set to 420 V on Top channels of A1515BTG boards (the ones generating electric field inside GEM foil holes);
- voltage OFF on Drift and Bot channels of A1515BTG boards (the ones generating electric field in the gas gaps);
- I_0 set to $I_0 = I_{b-420} + 20\,\mu\text{A}$, where I_{b-420} is the baseline current expected to flow in a given channel of the power supply, when that provides a voltage of 420 V. For the Drift and Bot channels $I_{b-420} = 0\,\mu\text{A}$ since no short circuit is present there, while for the Top electrodes this value corresponds to the current which flows in the power supply channel when 420 V are applied to the GEM foil.
- t_{trip} in the A1515BTG board is set to $t_{\text{trip}} = 3$ s.

Applying these settings, the GEM foils are kept with a high HV value applied and they can sustain a discharge with an amplitude of 20 µA above I_{b-420}, and lasting for less than $t_{\text{trip}} = 3$ s. This protection proved to be effective to improve operation of detectors in case of magnet ramp.

The only situation where the protection cannot be applied is in case of a fast discharge of the CMS magnet. In this case, the CMS Detector Safety System (DSS) powers off all the HV racks powering the GEM system, and to the GEM detectors. Two such events occurred in 2023. In both cases, no new short was observed to be generated. In the first case (22nd March 2023) HV was ON at $I_{\text{eq}} = 700\,\mu\text{A}$ and then got cut, while in the second case (16th August 2023) HV was already OFF before the magnet ramp.

An evaluation of the impact of magnet protection on the GEM operation is presented in table 7. Here, the number of short circuits generated per CMS magnet ramp is reported. To keep into account the number of short circuits already present in the system per year, this number has been normalized also to the number of foils (or chambers as alternative) not affected by any short circuit. The ratio R is defined as

$$R = \frac{N_s}{N_m \cdot N_h}, \tag{5.1}$$

2025 JINST 20 P05035

Table 7. Number of short circuits generated per year and related to CMS magnet ramps. In 2021, magnet protection was not in place and it was developed after the observation of short circuits generation during magnet operations. In this year, eight short circuits out of 9 related to magnet were generated when the HV was OFF. In the following two years, the HV was kept ON during magnet ramps. The top part of the table shows a number of short circuits developed per magnet ramp, normalized to the number of GEM foils not yet affected by any short circuit, before the first magnet ramp of the year. The bottom part of the table presents the same numbers, but normalized to the number of detectors whose GEM foils were not affected by any short circuit. In the 2023 data, a detector disconnected from HV is excluded from the count.

Year	CMS magnet ramps	Shorts generated	Affected foils	Healthy foils	Short per ramp per foil
2021	27	9	4	428	$(7.8 \pm 2.6) \cdot 10^{-4}$
2022	11	4	23	409	$(8.9 \pm 4.4) \cdot 10^{-4}$
2023	41	8	40	389	$(5.0 \pm 1.8) \cdot 10^{-4}$
Year	CMS magnet ramps	Shorts generated	Affected chambers	Healthy chambers	Short per ramp per chamber
2021	27	9	6	138	$(2.4 \pm 0.8) \cdot 10^{-3}$
2022	11	4	20	124	$(2.9 \pm 1.5) \cdot 10^{-3}$
2023	41	8	35	108	$(1.8 \pm 0.6) \cdot 10^{-3}$

where N_s is the number of short circuits generated per year due to magnet ramps, N_m the number of magnet ramps and N_h the number of healthy elements (GEM foils or chambers) before the first magnet ramp of the year.

Regarding the number of magnet ramps, we adopted the convention of defining a ramp as any variation in the magnetic field until the sign of its time derivative reverses. For example, if a magnet ramp up from 0 T to 3.8 T is interleaved by several pauses in the operation, it is considered a unique ramp-up.

In this preliminary calculation, it appears that the magnet protection procedure was effective in 2023, with a lower ratio of short circuits per ramp, in comparison to the previous years, despite an increased number of magnet ramps. It is nevertheless worthwhile to consider that not all chambers exhibit the same efficiency at identical HV working points, even when the production method is identical. Moreover, the probability of a new short circuit occurring on a GEM foil that has already experienced a short circuit may differ from the probability of a new short circuit occurring in a completely healthy foil. Similarly, the probability of a new short circuit occurring in a detector where at least one other GEM foil is affected by at least one short circuit may differ from the probability of a new short circuit occurring in a detector where no other foils are affected. It was not possible to distinguish these effects in the presented results, given that they are rare events and hard to reproduce in the laboratory. Finally, the probability of generating a short circuit may be increased by the presence of chemicals within the detector gas volume and by their quantity.

5.2 Re-map of the HV system

As mentioned in section 2.3, a short circuit in a GEM foil implies a lower voltage applied to the GEM foil, with respect to the value provided by the power supply. To compensate for the efficiency

2025 JINST 20 P05035

loss caused by the short circuit, it is necessary to account for the resulting voltage drop. This can be achieved by increasing the voltage supplied by the HV power supply.

Increasing the HV for a given channel on the power supply side implies that each detector fed by the same cable will undergo the same increase, so the two detectors which define a super-chamber, outlined in section 1. Nevertheless, the two detectors may be affected by short circuits affecting a different number of HV sectors in the same GEM foil (for example, GEM3 foil in Layer 1 detector has two HV sectors affected by a short circuit while Layer 2 has GEM3 foil affected by only one), or in different GEM foils (for example, Layer 1 is affected by a short circuit in GEM1 while Layer 2 is affected by a short circuit in GEM2). If the same HV compensation value is applied on the power supply on a given GEM foil, the two detectors may not be in the same gain configuration. For example, let's imagine a super-chamber where the Layer 1 detector is affected by a short circuit on foil GEM3, while Layer 2 is a totally healthy detector. Applying a compensation on the power supply side would indeed mean restoring the correct gain for Layer 1 detector, but Layer 2 would go to high gain configuration, exposing it to a higher discharge rate and a higher possibility of developing a short circuit, as described in section 4.4. The first step to handle the generation of these short circuits and have chambers with a similar gain performance (which means a similar muon detection efficiency), is to further pair them together. Because of this, a prerequisite to implement the HV compensation is to periodically re-map the HV system. The goal is to pair chambers with similar issues and power them with the same HV channel. In this way, those which have the same number of HV sectors affected by a short circuit in a given GEM foil, will be powered in pair by the same HV line. This result is obtained by re-organizing the connections in the patch panel shown in figure 6, and by introducing additional A1515BTG boards if needed.

The HV compensation mechanism is not applied yet. For the moment, we exercised to adapt the GEM system to handle the HV re-map, in particular in the GEM DCS.

The HV re-map implies that detectors with a similar gain are powered together, which allows to vary the HV working point of the whole chamber, without worrying of having very different gains on the two chambers in a pair.

The fact that chambers with similar gain are powered together is useful to study the muon detection efficiency as a function of the HV working point I_{eq} applied. Such a HV-scan study is performed once per year, collecting p-p collisions data at different I_{eq} for GE1/1 detectors. The goal of the HV-scan is to tune the HV working point of a given pair of chambers, paired together in the HV system, depending on their discharge rate and muon detection efficiency.

5.3 HV working point

As illustrated in section 3, the occurrence of frequent discharges impacts the stability of the detector during the operations. Additionally, they can lead to the generation of damages in the GEM foils, and in the readout channels of the front-end electronics [29]. In order to preserve the integrity of the detector from damages, it was decided to operate the chambers at a lower HV working point, $I_{eq} = 690\,\mu A$ in 2022. Consequently, the discharge rate in p-p collisions decreased, as shown in section 3. The discharge rate in a GEM detector indeed increases with the HV applied, as illustrated in [3]. The reduction of the HV working point had a contained effect on the detector efficiency, decreasing of $\sim 1\%$ respect to the efficiency obtained at the plateau. This calculation was done looking to the chambers not affected by short circuits, to not introduce additional effects in it. The effect of short circuits on the efficiency will instead be evaluated by a series of ongoing studies.

2025 JINST 20 P05035

Throughout 2022, the performances of several HV working points were analyzed during the HV-scan, to assess the muon detection efficiency of detectors during collisions and after the generation of several short circuits. The working point optimization is still in progress to reach the best compromise for the muon detection efficiency and the discharge rate. The dependence of discharge rate on the HV working point is now subject of a future study and one of the goals of 2024 HV scan.

6 Conclusion

The work presented in this paper focused on illustrating two topics important for the operations of GE1/1 detectors in CMS: the occurrence of discharges and the generation of short circuits in the GEM foils. The discharges affect the stability of the detector and increase the risk of developing a short circuit in a GEM foil, with the additional risk of generating damages in the front-end electronics.

During the first year of Run-3, their occurrence has been mitigated by lowering the HV working point of the chambers to $I_{\text{eq}} = 690\,\mu\text{A}$, stabilizing around one discharge per hour per chamber in 2022. This was done to better preserve the integrity of the detector and of the front-end electronics. A tuning of the working point is ongoing, depending on the chamber discharge rate, and on the HV working point needed to reach the efficiency plateau. In addition, it was observed that the discharge rate can decrease in time, suggesting a conditioning effect of some GEM holes affected by manufacturing imperfections.

The second main topic was to understand the phenomenology of generation of short circuits in the GEM foils and to develop safe operation procedures. Their generation seems to be favored by the occurrence of discharges and by the presence of potential pollutants inside the detectors, but this last point is still under investigation. The observations suggested to avoid long periods with HV OFF and too high HV working points during the restart operations, after the end of year technical stop. The other main situation when the generation of short circuits is more frequent is in case of variation of CMS magnetic field. During a magnet ramp, the detectors seem more prone to developing a short circuit in case of HV OFF and at the beginning or at the end of a magnet ramp. A protection mechanism for the magnet operations was deployed in the DCS, improving the operation of GE1/1 detectors in such situations. The studies also investigated the role played by the sign of the magnet ramp and the composition of the gas mixture. However, no clear relation was found.

Regarding the healing of short circuits, a significant fraction is removed by a gradual decrease of the drained current, suggesting the consumption of a resistive contact. This suggests the possible presence of pollutants inside of the detector, which could deposit on the GEM foils. First hints concerning this hypothesis came from three chambers extracted from CMS in January 2024, where, in two detectors, signs of oxidation on the readout plane were observed. For the GE1/1 production, a chromic-acid passivization was not applied while the chambers used during the aging tests had an extra layer of chromium on top of the base copper material, which during the aging tests showed no change in the detector performances [30, 31]. In any case, no issue in the stretching of the foils or any visible degradation of the mechanical components present inside the gas volume was found out in these three inspected chambers.

More information concerning the internal status of the detectors will be provided by a wider inspection of detectors, when the whole GE1/1 station will be extracted from CMS during the Long Shutdown 3 upgrade phase.

Finally, a preliminary analysis showed as the discharge rate increases with the instantaneous luminosity of the LHC beams collisions, and the first results of an ongoing study showed a linear

2025 JINST 20 P05035

dependence [32]. The combination of the results provided by the study of these dependencies is helping us to gain a full understanding of the physics playing a role in the detector operation. The analysis of muon detection efficiencies in GE1/1 detectors and on the discharge rate data observed during the HV scan of 2024 is being used to optimize the HV working point and all the knowledge on detector operations provided useful feedback for the production of new GEM detectors (GE2/1 and ME0).

Acknowledgments

We gratefully acknowledge support from CERN, FRS-FNRS (Belgium), FWO-Flanders (Belgium), BSF-MES (Bulgaria), MOST and NSFC (China), BMBF (Germany), DAE (India), DST (India), INFN (Italy), NRF (Korea), and DOE (U.S.A.). We are gratefully thank also B. Cure (CERN) for the support provided to the GEM team for the data collection.

References

[1] CMS collaboration, *The CMS Experiment at the CERN LHC*, 2008 *JINST* **3** S08004.

[2] LHC long term schedule, http://lhc-commissioning.web.cern.ch/schedule/LHC-long-term.htm.

[3] F. Sauli, *The gas electron multiplier (GEM): Operating principles and applications*, *Nucl. Instrum. Meth. A* **805** (2016) 2.

[4] M. Titov and L. Ropelewski, *Micro-pattern gaseous detector technologies and RD51 Collaboration*, *Mod. Phys. Lett. A* **28** (2013) 1340022.

[5] A. Colaleo, A. Safonov, A. Sharma and M. Tytgat, *CMS Technical Design Report for the Muon Endcap GEM Upgrade*, CERN-LHCC-2015-012 (2015).

[6] G. Apollinari, O. Brüning, T. Nakamoto and L. Rossi, *High Luminosity Large Hadron Collider HL-LHC*, *CERN Yellow Rep.* **5** (2015) 1 [arXiv:1705.08830].

[7] CMS collaboration, *The Phase-2 Upgrade of the CMS Muon Detectors*, CERN-LHCC-2017-012, CERN, Geneva (2017) [DOI:10.17181/CERN.5T9S.VPMI].

[8] M. Abbas et al., *Quality control of mass-produced GEM detectors for the CMS GE1/1 muon upgrade*, *Nucl. Instrum. Meth. A* **1034** (2022) 166716 [arXiv:2203.12037].

[9] F. Fallavollita, *Triple-Gas Electron Multiplier technology for future upgrades of the CMS experiment: construction and certification of the CMS GE1/1 detectors and longevity studies*, Ph.D. thesis, Pavia University, Pavia, Italy (2019), https://iris.unipv.it/handle/11571/1239046.

[10] G. Mocellin, *Performance of the GE1/1 detectors for the upgrade of the CMS muon forward system*, Ph.D. thesis, RWTH Aachen University, Aachen, Germany (2022).

[11] CMS collaboration, *The Phase-2 Upgrade of the CMS Level-1 Trigger*, CERN-LHCC-2020-004, CERN, Geneva (2020).

[12] P. Aspell et al., *VFAT3: A Trigger and Tracking Front-end ASIC for the Binary Readout of Gaseous and Silicon Sensors*, in the proceedings of the *2018 IEEE Nuclear Science Symposium and Medical Imaging Conference*, Sydney, Australia, November 10–17 (2018) [DOI:10.1109/NSSMIC.2018.8824655].

[13] CAEN, *A1515B*, https://www.caen.it/products/a1515b/.

[14] CAEN, *A3016*, https://www.caen.it/products/a3016/.

[15] A. Deisting et al., *Secondary discharge studies in single and multi GEM structures*, *Nucl. Instrum. Meth. A* **937** (2019) 168 [arXiv:1901.06035].

2025 JINST 20 P05035

[16] P. Gasik, *Discharge probability studies with multi-GEM detectors for the ALICE TPC Upgrade*, *PoS* **MPGD2017** (2019) 031 [arXiv:1807.02979].

[17] F. Fallavollita, D. Fiorina and J.A. Merlin, *Advanced Aging study on Triple-GEM Detectors*, *J. Phys. Conf. Ser.* **1498** (2020) 012038.

[18] H. Raether, *Electron Avalanches and Breakdown in Gases*, Butterworths (1964), ISBN: 9780598450210.

[19] M. Abbas et al., *Detector Control System for the GE1/1 slice test*, 2020 *JINST* **15** P05023.

[20] D. Fiorina, *R&D on Triple-GEM detectors for the optimal and safe operation in the CMS experiment*, Ph.D. thesis, Pavia University, Pavia, Italy (2022).

[21] S. Calzaferri, *Study of the operation and trigger performance of GEM detectors in the CMS experiment*, Ph.D. thesis, Pavia University, Pavia, Italy (2022), https://iris.unipv.it/handle/11571/1452086.

[22] S. Calzaferri, *Study of discharges in the CMS GEM GE1/1 station with LHC beam*, 2023 *JINST* **18** C06016.

[23] S. Calzaferri, *Analysis of discharge events in the CMS GE1/1 GEM detectors in presence of LHC beam*, 2024 *JINST* **19** C02003.

[24] V. Peskov and P. Fonte, *Research on discharges in micropattern and small gap gaseous detectors*, arXiv:0911.0463.

[25] S. Calzaferri and D. Fiorina, *Commissioning and operation in magnetic field of CMS GE1/1 station*, *Nucl. Instrum. Meth. A* **1048** (2023) 167998.

[26] M. Abbas et al., *Impact of magnetic field on the stability of the CMS GE1/1 GEM detector operation*, 2023 *JINST* **18** P11029.

[27] CMS collaboration, *Precise Mapping of the Magnetic Field in the CMS Barrel Yoke using Cosmic Rays*, 2010 *JINST* **5** T03021 [arXiv:0910.5530].

[28] S. Calzaferri, *Operation of CMS GE1/1 GEM detectors in Run-3*, *PoS* **ICHEP2024** (2025) 896.

[29] F. Ivone, *Discharge mitigation strategies for the CMS GE1/1 Triple-GEM detectors*, 2020 *JINST* **15** C05009.

[30] J.A. Merlin, *Study of long-term sustained operation of gaseous detectors for the high rate environment in CMS*, Ph.D. thesis, Strasbourg University, Strasbourg, France (2016), CERN-THESIS-2016-041.

[31] D. Fiorina, *Advanced aging study on Triple GEMs for CMS GE2/1 and ME0*, M.Sc. thesis,, Pavia University, Pavia, Italy (2018), CERN-THESIS-2018-472.

[32] S. Calzaferri, *Study of discharges observed in the CMS GE1/1 station during LHC Run-3*, *Nucl. Instrum. Meth. A* **1075** (2025) 170330.

2025 JINST 20 P05035

The GEM group of the CMS collaboration

M. Abbas[o], S. Abbott[ai], M. Abbrescia[t], H. Abdalla[j,l], A. Abdelalim[j,m], S. AbuZeid[j,k], D. Aebi[ah], A. Ahmad[ad], W. Ahmed[ad], C. Aimè[x,1], T. Akhter[ah], G. Alasfour[ac], M. Ali[a], B. Alsufyani[am], A. Aravind[al], C. Aruta[t,2], I. Asghar[ad], P. Aspell[ag], C. Avila[h], Y. Ban[f], R. Band[ai,3], S. Bansal[q], N. Beni[p,ag], L. Benussi[v], T. Beyrouthy[ac], V. Bhatnagar[q], M. Bianco[ag], S. Bianco[v], K. Black[al], O. Bouhali[ah,4], S. Brachet[ag], A. Braghieri[x], M. Buonsante[t], S. Butalla[am], A. Cagnotta[w,*], S. Calzaferri[x,*], R. Campagnola[v], M. Caponero[v], F. Cassese[w], N. Cavallo[w], B. Chauhan[q], S.S. Chauhan[q], B. Choudhary[r], M. Citron[ai], S. Colafranceschi[v], A. Colaleo[t], A. Conde Garcia[ag], A. Datta[ak], A. De Iorio[w], G. De Lentdecker[a], G. De Robertis[t], W. Dharmaratna[af], C. Di Fraia[w], T. Elkafrawy[am], R. Erbacher[ai], P. Everaerts[al], F. Fabozzi[w], F. Fallavollita[ag,5], L. Favilla[w], D. Fiorina[x,6], M. Franco[t], C. Galloni[al], Y. Gharbia[ac], P. Giacomelli[u], S.G. Gigli[x], J. Gilmore[ah], G. Gokbulut[c], R. Hadjiiska[d], T. Hebbeker[n], K. Hoepfner[n], M. Hohlmann[am], Y. Hong[b,c], H. Hoorani[ad], T. Huang[ah], P. Iaydjiev[d], A. Iorio[w], F. Ivone[n], W. Jang[ab], J. Jaramillo[i], E. Juska[ah], B. Kailasapathy[ae,7], T. Kamon[ah], Y. Kang[ab,8], P. Karchin[aj], S. Keshri[e], D. Kim[ab], H. Kim[ah], J. Kim[z], M. Kim[aa], S. Kim[ab], B. Ko[ab], A. Kumar[r], S. Kumar[q], N. Lacalamita[t], J.S.H. Lee[ab], Q. Li[f], Z. Li[f], F. Licciulli[t], L. Lista[w], K. Liyanage[af], F. Loddo[t], L. Longo[t], M. Luhach[q], M. Maggi[t], N. Majumdar[s], K. Malagalage[ae], S. Malhotra[ah], S. Martiradonna[t], J. Merlin[y], M. Merschmeyer[n], M. Misheva[d], G. Mocellin[ai], S. Muhammad[ad], S. Mukhopadhyay[s], M. Naimuddin[r], F. Nenna[t], S. Nuzzo[t], R. Oliveira[ag], S. Ostrom[ai], M. Otkur[ac], E. Paoletti[v], P. Paolucci[w], I.C. Park[ab], G. Passeggio[w], A. Pellecchia[t], N. Perera[af], L. Petre[al], D. Piccolo[v], D. Pierluigi[v], R. Radogna[t], A. Ranieri[t], G. Rashevski[d], D. Rathjens[ah], B. Regnery[ai,9], C. Rendon[c], C. Riccardi[x], M. Rodríguez[i], B. Rossi[w], P. Rout[s], A.A. Ruales[i], J.D. Ruiz-Àlvarez[i], A. Russo[v], A. Safonov[ah], A.K. Sahota[q], M. Saini[r], D. Saltzberg[ak], G. Saviano[v], A. Sharma[ag], T. Sheokand[q], M. Shopova[d], F.M. Simone[t], J. Singh[q], K. Skovpen[c], U. Sonnadara[ae], A. Stamerra[t], G. Sultanov[d], Z. Szillasi[p,ag], D. Teague[al], R. Tesauro[v], D. Teyssier[p], S. Thakur[e], D. Troiano[t], M. Tytgat[b,c], I. Vai[x], R. Venditti[t], P. Verwilligen[t], W. Vetens[al], A.K. Virdi[q], P. Vitulo[x], A. Wajid[ad], D. Wang[f], A. Warden[al], I.J. Watson[ab], N. Wickramage[af], D.D.C. Wickramarathna[ae], E. Yanes[am], U. Yang[z], Y. Yang[a], I. Yoon[z], Z. You[g], I. Yu[aa], S. Zaleski[n], A. Zaza[t], C. Zhou[f]

[a] *Université Libre de Bruxelles, Bruxelles, Belgium*
[b] *Vrije Universiteit Brussel, Brussels, Belgium*
[c] *Ghent University, Ghent, Belgium*
[d] *Institute for Nuclear Research and Nuclear Energy, Bulgarian Academy of Sciences, Sofia, Bulgaria*
[e] *Instituto de Alta Investigación, Universidad de Tarapacá, Casilla 7D, Arica, Chile*
[f] *Peking University, Beijing, China*
[g] *Sun Yat-Sen University, Guangzhou, China*
[h] *University de Los Andes, Bogota, Colombia*
[i] *Universidad de Antioquia, Medellin, Colombia*
[j] *Academy of Scientific Research and Technology - ENHEP, Cairo, Egypt*
[k] *Ain Shams University, Cairo, Egypt*
[l] *Cairo University, Cairo, Egypt*
[m] *Helwan University, also at Zewail City of Science and Technology, Cairo, Egypt*
[n] *RWTH Aachen University, III. Physikalisches Institut A, Aachen, Germany*
[o] *Karlsruhe Institute of Technology, Karlsruhe, Germany*
[p] *Institute for Nuclear Research ATOMKI, Debrecen, Hungary*
[q] *Panjab University, Chandigarh, India*
[r] *Delhi University, Delhi, India*
[s] *Saha Institute of Nuclear Physics, Kolkata, India*
[t] *Politecnico di Bari, Università di Bari and INFN Sezione di Bari, Bari, Italy*

2025 JINST 20 P05035

[u] Università di Bologna and INFN Sezione di Bologna, Bologna, Italy
[v] Laboratori Nazionali di Frascati INFN, Frascati, Italy
[w] Università di Napoli and INFN Sezione di Napoli, Napoli, Italy
[x] Università di Pavia and INFN Sezione di Pavia, Pavia, Italy
[y] Hanyang University, Seoul, Korea
[z] Seoul National University, Seoul, Korea
[aa] Sungkyunkwan University, Gyeonggi, Republic of Korea
[ab] University of Seoul, Seoul, Korea
[ac] College of Engineering and Technology, American University of the Middle East, Dasman, Kuwait
[ad] National Center for Physics, Islamabad, Pakistan
[ae] University of Colombo, Colombo, Sri Lanka
[af] University of Ruhuna, Matara, Sri Lanka
[ag] CERN, Geneva, Switzerland
[ah] Texas A&M University, College Station, U.S.A.
[ai] University of California, Davis, U.S.A.
[aj] Wayne State University, Detroit, U.S.A.
[ak] University of California, Los Angeles, U.S.A.
[al] University of Wisconsin, Madison, U.S.A.
[am] Florida Institute of Technology, Melbourne, U.S.A.

[*] Corresponding author
[1] Now at Università di Pisa and INFN Sezione di Pisa, Pisa, Italy
[2] Now at University of Florida, Gainesville, U.S.A.
[3] Now at University of Notre Dame, Notre Dame, U.S.A.
[4] Also at Hamad Bin Khalifa University, Doha, Qatar
[5] Now at Max Planck Institut für Physik, München, Germany
[6] Now at Gran Sasso Science Institute and INFN Laboratori Nazionali del Gran Sasso, L'Aquila, Italy
[7] Also at Trincomalee Campus, Eastern University, Nilaveli, Sri Lanka
[8] Now at Sejong University, Seoul, Korea
[9] Now at Karlsruhe Institute of Technology, Karlsruhe, Germany

2025 JINST 20 P05035